Wavefront Reconstruction in Adaptive Optics Systems using Nonlinear Multivariate Splines

Cornelis de Visser,[1,*] and Michel Verhaegen[2]

[1]*Department of Control & Simulation, Delft University of Technology,*
Kluyverweg 1, 2629 HS, Delft, The Netherlands

[2]*Delft Center for Systems and Control, Delft University of Technology,*
Mekelweg 2, 2628 CD, Delft, The Netherlands

[*]*Corresponding author: c.c.devisser@tudelft.nl*

This paper presents a new method for zonal wavefront reconstruction with application to adaptive optics systems. This new method, indicated as SABRE, uses bivariate simplex B-spline basis functions to reconstruct the wavefront using local wavefront slope measurements. The SABRE enables wavefront reconstruction on non-rectangular and partly obscured sensor grids, and is not subject to the waffle mode. The performance of SABRE is compared to that of the finite difference method in numerical experiments using data from a simulated Shack-Hartmann lenslet array. The results show that SABRE offers superior reconstruction accuracy and noise rejection capabilities compared to the finite difference method.

OCIS codes: 010.1080, 010.7350, 010.1285, 000.3860, 000.4430, 350.1260.

1. Introduction

Active control of the phase of the photon wavefront for aberration compensation is essential to many photonics applications in science and engineering. It is the field of adaptive optics (AO) that is concerned with measuring and reshaping the wavefront phase in real-time. One of the most important applications of AO is in the field of astronomy, where AO systems are used in optical telescopes to compensate for atmospheric turbulence induced wavefront aberrations which degrade the quality of scientific observations [2].

Any AO system can be divided into three parts. The first is the wavefront sensing part in which a wavefront sensor (WFS) measures the slopes or curvature of the wavefront. The

second part is the wavefront reconstruction (WFR) part which uses the WFS measurements to reconstruct the global wavefront. The third part is the control part which uses the reconstructed wavefront to generate control laws for the actuators of a deformable mirror (DM).

Wavefront reconstruction is a complicated process because current wavefront sensors (WFS) cannot measure the wavefront directly, but rather its slope or its curvature [12, 15, 27, 29]. This means that the global wavefront must be estimated from WFS measurements, which are often contaminated with sensor noise and biased due to unmodelled parts in the sensor-phase relationship. The WFR estimation problem, together with the large scale of modern WFS arrays lead to a computationally expensive process which is challenging to implement in real-time control systems. The three most important aspects of any WFR method are its reconstruction accuracy, its computational efficiency, and its ability to deal with real-life sensor and actuator geometries. There exist many different WFR methods, which can roughly be divided into zonal (local) methods and modal (global) methods.

One of the best known and most widely used zonal WFR methods is the finite difference (FD) method, which comes in a number of different forms [12, 15, 29]. The FD method is characterized by the fact that it assumes that the wavefront is defined on a rectangular grid with linear polynomials interpolating between grid points (phase points). Fueled by the development of a new generation of extremely large optical telescopes, innovations in FD methods are mainly focused on increasing their computational efficiency [18, 19]. Examples of such innovations are a computationally efficient sparse matrix inversion method by Vogel and Ellerbroek [11, 30], and a multigrid preconditioned conjugate-gradient method by Gilles et al. and Vogel and Yang [13, 31]. More recently, Rosensteiner presented a cumulative reconstruction method based on line integrals which further reduces computational complexity [28].

Modal methods based on polynomials in polar coordinates, such as the Zernike polynomials and Karhoenen-Loève (KL) functions, are widely used in AO systems [5, 23]. A more recent type of modal methods are the Fourier domain methods, which have been developed for the purpose of improving the computational efficiency of the WFR problem [25, 26]. More recently, Hampton et al. introduced a modal WFR method based on Haar wavelets which was shown to have a linear computational complexity [14].

While current WFR methods are well established and proven in practice, they suffer from a lack of generality. FD methods on the one hand are relatively straightforward to implement on rectangular WFS arrays, but are essentially linear while the physical wavefront is certainly not linear. Additionally, it is not trivial to implement FD methods on AO systems with non-rectangular WFS arrays and obstructions in the field of view of the telescope pupil (e.g. spiders). Modal methods based on Zernike and Karhoenen-Loève polynomials have a limited approximation power and are subject to oscillations on the edges of the domain

(i.e. Runge's phenomenon). Additionally, the polar nature of Zernike and Karhoenen-Loève polynomial methods makes their implementation on non-circular WFS arrays non-trivial [5]. Fourier methods on the other hand have a transparent implementation on rectangular WFS grids. However, on non-rectangular, non-homogeneous, or partially obscured WFS grids, their implementation becomes more complex [25].

The objective of this paper is to present a new method for wavefront reconstruction from wavefront slope measurements that uses bivariate simplex B-splines inside a linear regression framework [1, 8–10, 21]. This new method, which we call SABRE (Spline based ABerration REconstruction) aims to be a truly general WFR method. In essence, SABRE locally models the wavefront with linear and nonlinear simplex B-spline basis functions on triangular subpartitions of the WFS domain using local WFS measurements. While this paper presents only a least squares estimator for the simplex spline coefficients (i.e. B-coefficients), it is compatible with any more advanced linear regression parameter estimation technique.

SABRE has five important advantages over other WFR methods. Firstly, SABRE is invariant of WFS geometry in the sense that it can be used without any modification on non-rectangular, non-homogeneous (misaligned), and partially obscured sensor grids. This is a significant advantage in real life AO setups, where non-rectangular WFS grids with misaligned lenslet images are often encountered. Secondly, SABRE allows wavefront reconstruction using nonlinear basis functions resulting in a more accurate approximation of the physical wavefront. Thirdly, SABRE has an inherent noise smoothing capability which makes it highly resilient to sensor noise. Fourthly, in contrast to the Fried-geometry based FD method, the SABRE is not subject to the waffle mode [24, 32]. Finally, the local nature of SABRE means that it can be implemented on multi-core hardware resulting in a distributed SABRE (D-SABRE) that can significantly increase computational efficiency. This paper will focus primarily on the first four of these advantages, while the distributed SABRE will be explored in a forthcoming paper.

This paper is outlined as follows. In Sec. 2 we provide preliminaries on bivariate simplex B-splines as they are central to the new WFR method. Then, in Sec. 3 we introduce the SABRE method, and present a least squares estimator for estimating the SABRE model parameters. Additionally, we show in Sec. 3 that for fundamental reasons the SABRE is not subject to the waffle mode. In Sec. 4 the results from a number of numerical experiments utilizing a Fourier optics based Shack-Hartmann sensor simulation are presented. In the experiments it is shown that SABRE can reconstruct nonlinear wavefronts that are closer to physical reality than wavefronts produced by any FD method. Subsequently, the ability of SABRE to reconstruct wavefronts on non-rectangular domains is demonstrated. In Sec. 5 we conclude the paper, and provide pointers for future research.
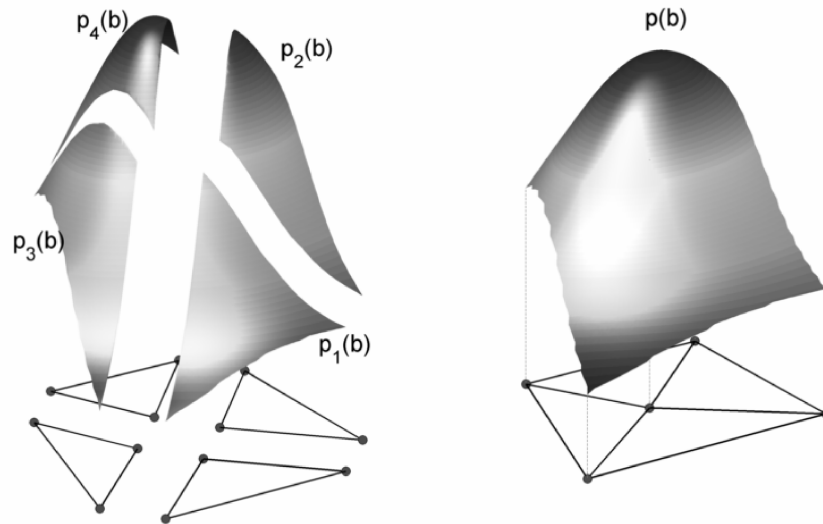
Fig. 1: The principle of the multivariate simplex spline; a 5th degree spline function with C^1 continuity defined on 4 triangles with (left) the 4 individual spline pieces ($p_1(b)$, $p_2(b)$, $p_3(b)$, and $p_4(b)$), and (right) the global spline function $p(b)$ formed by combining the 4 spline pieces.

2.   Preliminaries on Multivariate Simplex B-Splines

To provide the reader with a basic understanding of the theory behind SABRE a brief introduction into the theory of bivariate simplex B-splines is given. For a more complete and general introduction into the theory of multivariate simplex B-splines we refer to [21].

2.A.   The 2-Simplex and Barycentric Coordinates

Let t be a 2-simplex (triangle) formed by the convex hull of its 3 non-degenerate vertices $(\mathbf{v}_0, \mathbf{v}_1, \mathbf{v}_2) \in \mathbb{R}^2$ as follows:

$$t := \left\langle \begin{bmatrix} \mathbf{v}_{0_x} \\ \mathbf{v}_{0_y} \end{bmatrix}, \begin{bmatrix} \mathbf{v}_{1_x} \\ \mathbf{v}_{1_y} \end{bmatrix}, \begin{bmatrix} \mathbf{v}_{2_x} \\ \mathbf{v}_{2_y} \end{bmatrix} \right\rangle \quad \in \mathbb{R}^2 \tag{1}$$

The basis polynomials of the simplex B-splines are functions in terms of barycentric coordinates. The Barycentric coordinate system is a local coordinate system which is defined on an individual simplex. If $\mathbf{x} \in \mathbb{R}^2$ is a point on the Cartesian plane, then the normalized barycentric coordinate $\mathbf{b} \in \mathbb{R}^3$ of $\mathbf{x}$ with respect to the triangle t can be determined using the following equations:

$$\begin{bmatrix} x_1 \\ x_2 \end{bmatrix} = \begin{bmatrix} \mathbf{v}_{0_x} & \mathbf{v}_{1_x} & \mathbf{v}_{2_x} \\ \mathbf{v}_{0_y} & \mathbf{v}_{1_y} & \mathbf{v}_{2_y} \end{bmatrix} \begin{bmatrix} b_0 \\ b_1 \\ b_2 \end{bmatrix}, \quad b_0 + b_1 + b_2 = 1, \tag{2}$$

The condition $b_0 + b_1 + b_2 = 1$ is a normalization condition, which ensures that any $\mathbf{x} \in \mathbb{R}^2$ has a unique representation $\mathbf{b} \in \mathbb{R}^3$ in barycentric coordinate space. Now define the normalized simplex vertex matrix $\mathbf{V}$ as follows:

$$\mathbf{V} := \begin{bmatrix} (\mathbf{v}_{1_x} - \mathbf{v}_{0_x}) & (\mathbf{v}_{2_x} - \mathbf{v}_{0_x}) \\ (\mathbf{v}_{1_y} - \mathbf{v}_{0_y}) & (\mathbf{v}_{2_y} - \mathbf{v}_{0_y}) \end{bmatrix} \tag{3}$$

Using the matrix $\mathbf{V}$ from (3), the barycentric coordinate $\mathbf{b} = (b_0, b_1, b_2) \in \mathbb{R}^3$ of the Cartesian coordinate $\mathbf{x} \in \mathbb{R}^2$ is calculated as follows:

$$\begin{aligned} \begin{bmatrix} b_1 \\ b_2 \end{bmatrix} &= \mathbf{V}^{-1} \begin{bmatrix} x_1 \\ x_2 \end{bmatrix} \\ b_0 &= 1 - b_1 - b_2, \end{aligned} \tag{4}$$

In the remainder of the paper, we shall use the following shorthand notation for the Cartesian-to-barycentric coordinate transformation from $\mathbf{x} \in \mathbb{R}^2$ to $\mathbf{b} \in \mathbb{R}^3$ on the triangle t:

$$b(\mathbf{x}) := (b_0, b_1, b_2) \in \mathbb{R}^3, \quad \mathbf{x} \in \mathbb{R}^2 \tag{5}$$

2.B. Triangulations of Simplices

The approximation power of the multivariate simplex B-spline can be increased by combining many simplices into a structure called a triangulation. A triangulation $\mathcal{T}$ is a special partitioning of a domain into a set of J non-overlapping simplices:

$$\mathcal{T} := \bigcup_{i=1}^{J} t_i, \quad t_i \cap t_j \in \left\{\emptyset, \tilde{t}\right\}, \quad \forall t_i, t_j \in \mathcal{T}, \tag{6}$$

with the edge simplex $\tilde{t}$ either a line (1-simplex), or a vertex (0-simplex) in the case of a 2-dimensional triangulation consisting of triangles.

A number of algorithms can be used to create triangulations from a given set of vertices. The most widely known of these is the Delaunay triangulation method, which has a standard implementation in Matlab. The triangulations used in this paper were all created with a different (non-Delaunay) technique based on the grid cell subdivision scheme introduced in [8].

2.C. Basis functions of the simplex B-splines

The basis polynomials of the simplex B-splines are Bernstein polynomials in terms of barycentric coordinates. The basis polynomials are derived using the multinomial theorem, which states that any polynomial of total degree d can be expanded into a sum of monomials. In $\mathbb{R}^3$ the result of the multinomial theorem is the following:

$$(b_0 + b_1 + b_2)^d = \sum_{\kappa_0+\kappa_1+\kappa_2=d} \frac{d!}{\kappa_0!\kappa_1!\kappa_2!} b_0^{\kappa_0} b_1^{\kappa_1} b_2^{\kappa_2}, \tag{7}$$

with $\kappa = (\kappa_0, \kappa_1, \kappa_2)$ a *multi-index* with the properties:

$$|\kappa| = \kappa_0 + \kappa_1 + \kappa_2 = d, \quad \kappa_0 \geq 0, \kappa_1 \geq 0, \kappa_2 \geq 0 \tag{8}$$

The Bernstein basis polynomials of the simplex B-splines are defined as the individual monomials in (7), with the additional rule that they are equal to 0 by definition when the evaluation point $\mathbf{x}$ is outside of the triangle t:

$$B_\kappa^d(b(\mathbf{x})) := \begin{cases} \frac{d!}{\kappa_0!\kappa_1!\kappa_2!} b_0^{\kappa_0} b_1^{\kappa_1} b_2^{\kappa_2} & , \mathbf{x} \in t \\ 0 & , \mathbf{x} \notin t \end{cases} \tag{9}$$

Any polynomial $p(b(\mathbf{x}))$ of degree d on a simplex t can be written as a linear combination of basis polynomials in what is known as the *B-form* as follows [7]:

$$p(b(\mathbf{x})) := \begin{cases} \sum_{|\kappa|=d} c_\kappa^t B_\kappa^d(b(\mathbf{x})) & , \mathbf{x} \in t \\ 0 & , \mathbf{x} \notin t \end{cases} \tag{10}$$
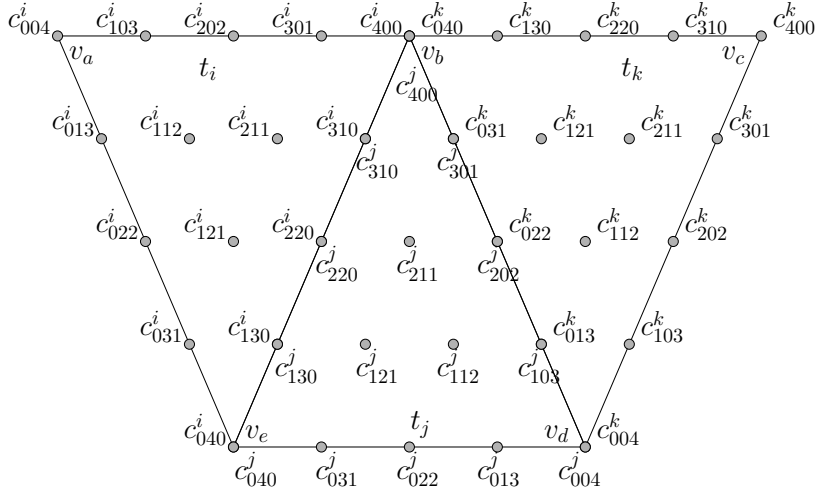
Fig. 2: B-net for a 4th degree spline function on a triangulation consisting of the 3 triangles t_i, t_j and t_k.

with c_κ^t the *B-coefficients* which uniquely determine the polynomial $p(b(\mathbf{x}))$ on the triangle t. The B-coefficients have a special geometric ordering inside their parent simplex, see Fig. 2. This ordering is called the *B-net*, and is essential for defining continuity between simplices, and for enforcing local external constraints on the simplex B-spline function [9, 10, 21].

The total number of B-coefficients and basis polynomials is equal to $\hat{d}$, which for the 2-dimensional case and a given degree d is given by:

$$\hat{d} := \frac{(d+2)!}{2d!}. \tag{11}$$

2.D.   *Vector formulations of the B-form*

In [9] a vector formulation of the B-form from (10) was introduced. With (5) the vector formulation for a B-form polynomial $p(b(\mathbf{x}))$ in barycentric $\mathbb{R}^3$ is:

$$p(b(\mathbf{x})) := \begin{cases} \mathbf{B}^d(b(\mathbf{x})) \cdot \mathbf{c}^t & , \mathbf{x} \in t \\ 0 & , \mathbf{x} \notin t \end{cases}, \tag{12}$$

with $b(\mathbf{x})$ the barycentric coordinate of the Cartesian $\mathbf{x}$ according to (5).

The row vector $\mathbf{B}^d(b(\mathbf{x}))$ in (12) is a vector which is constructed from individual basis

7

polynomials which are sorted lexicographically according to [16]:

$$\mathbf{B}^d(b(\mathbf{x})) \quad := \quad \begin{bmatrix} \mathbf{B}_{d,0,0}^d(b(\mathbf{x})) & \mathbf{B}_{d-1,1,0}^d(b(\mathbf{x})) & \cdots \\ \cdots & \mathbf{B}_{0,1,d-1}^d(b(\mathbf{x})) & \mathbf{B}_{0,0,d}^d(b(\mathbf{x})) \end{bmatrix} \quad \in \mathbb{R}^{1\times\hat{d}}.$$

(13)

The column vector $\mathbf{c}^t$ the vector of lexicographically sorted B-coefficients on the triangle t:

$$\mathbf{c}^t = [c_{d,0,0} \quad c_{d-1,1,0} \quad \cdots \quad c_{0,1,d-1} \quad c_{0,0,d}]^\top \quad \in \mathbb{R}^{\hat{d}\times 1}.$$

(14)

For example, for a B-form polynomial $p(b(\mathbf{x}))$ of degree $d = |\kappa| = 1$ in Barycentric $\mathbb{R}^3$ on the triangle t we have $\kappa \in \{(1,0,0),(0,1,0),(0,0,1)\}$. In this case the vector formulation of the B-form from (12) is:

$$\begin{aligned} p(b(\mathbf{x})) \quad &= \quad \mathbf{B}^1(b(\mathbf{x})) \cdot \mathbf{c}^t \\ &= \quad [b_0^1 b_1^0 b_2^0 \quad b_0^0 b_1^1 b_2^0 \quad b_0^0 b_1^0 b_2^1][c_{1,0,0}^t \quad c_{0,1,0}^t \quad c_{0,0,1}^t]^\top. \end{aligned}$$

The simplex B-spline function $s_d^r(b(\mathbf{x}))$ of degree d and continuity order r, defined on a triangulation $\mathcal{T}_J$ consisting of J triangles, is defined as follows:

$$s_d^r(b(\mathbf{x})) := \mathbf{B}^d \cdot \mathbf{c} \quad \in \mathbb{R}, \mathbf{x} \in \mathcal{T}_J$$

(15)

where the continuity order r, also denoted by C^r, signifies that all derivatives up to order r of two B-form polynomials defined on two neighboring triangles are equal *on the edge between the two triangles*. For example, C^0 continuity means that only the values of the B-form polynomials are equal on an edge between two neighboring triangles, while C^1 continuity means that both the first order derivatives and the values of the B-form polynomials match on the edge.

In (15), $\mathbf{B}^d$ is the global vector of basis polynomials which is constructed using (13) as follows:

$$\mathbf{B}^d := [\begin{array}{cccc} \mathbf{B}_{t_1}^d(b(\mathbf{x})) & \mathbf{B}_{t_2}^d(b(\mathbf{x})) & \cdots & \mathbf{B}_{t_J}^d(b(\mathbf{x})) \end{array}] \quad \in \mathbb{R}^{1\times J\cdot\hat{d}}$$

(16)

Note that according to (12) we have $\mathbf{B}_{t_j}^d(b(\mathbf{x})) = 0$ for all evaluation locations $\mathbf{x}$ that are located outside of the triangle t_j. The result of this is that the global vector of basis polynomials $\mathbf{B}^d$ is a sparse vector.

The global vector of B-coefficients $\mathbf{c}$ in (15) is constructed as follows:

$$\mathbf{c} := \begin{bmatrix} \mathbf{c}^{t_1\top} & \mathbf{c}^{t_2\top} & \cdots & \mathbf{c}^{t_J\top} \end{bmatrix}^\top \quad \in \mathbb{R}^{J\cdot\hat{d}\times 1}$$

(17)

with each $\mathbf{c}^{t_j}$ a per-simplex vector of lexicographically sorted B-coefficients from (14).

2.E. Spline Spaces

A spline space is defined as the space of all spline functions s_d^r of a given degree d and continuity order r on a given triangulation $\mathcal{T}$. Such spline spaces have been well studied in the past, see e.g. [20–22]. We use the definition of the spline space from [21]:

$$S_d^r(\mathcal{T}) := \{s_d^r \in C^r(\mathcal{T}) : s_d^r|_t \in \mathbb{P}_d, \ \forall t \in \mathcal{T}\} \tag{18}$$

with $\mathbb{P}_d$ the space of polynomials of degree d.

2.F. Continuity between Simplices

By definition, a spline function is a piecewise defined polynomial function with a predefined continuity order between its polynomial pieces. The continuity order r signifies that all m^{th} order derivatives, with $0 \leq m \leq r$, of two B-form polynomials defined on two neighboring triangles are equal on the edge between the two triangles. For simplex B-splines, continuity between neighboring triangles is enforced by *continuity conditions*.

The principle of the continuity conditions in Cartesian $\mathbb{R}^2$ is the following. Let two neighboring triangles t_i and t_j, differing by only the vertex $\mathbf{w}$, be defined as follows:

$$t_i := \langle \mathbf{v}_0, \mathbf{v}_1, \mathbf{w} \rangle, \ \ t_j := \langle \mathbf{v}_0, \mathbf{v}_1, \mathbf{v}_2 \rangle \tag{19}$$

Then t_i and t_j meet along the line $\tilde{t}$ given by:

$$\tilde{t} := t_i \cap t_j = \langle \mathbf{v}_0, \mathbf{v}_1, \rangle \tag{20}$$

The formulation for the continuity conditions for C^r continuity between t_i and t_j is the following [1, 21]:

$$-c_{(\kappa_0, \kappa_1, m)}^{t_i} + \sum_{|\gamma|=m} c_{(\kappa_0, \kappa_1, 0)+\gamma}^{t_j} B_\gamma^m(b(\mathbf{w})) = 0, \ \ 0 \leq m \leq r \tag{21}$$

with $\gamma = (\gamma_0, \gamma_1, \gamma_2)$ a multi-index independent of κ.

It was shown in [9] that the formulation provided in (21) is only accurate for specific B-net orientations, such as that of t_i and t_j in Fig. 2. A more general formulation of the continuity conditions requires the utilization of a B-net orientation rule such as that introduced in [8].

For C^r continuity there are a total of Q continuity conditions of the form (21) per edge:

$$Q := \sum_{m=0}^r (d - m + 1) \tag{22}$$

The continuity conditions for all E edges are collected into a single set of linear equations:

$$\mathbf{Hc} = 0 \tag{23}$$

9

In (23), the matrix $\mathbf{H} \in \mathbb{R}^{EQ \times J\hat{d}}$ is the so-called global smoothness matrix. Each row in $\mathbf{H}$ contains a single continuity condition. The vector $\mathbf{c}$ is the *global* vector of B-coefficients from (17). Constructing $\mathbf{H}$ is not a trivial task; for particular details on its construction we refer the reader to [8, 9, 21].

2.G. The matrix form of the directional derivative

In [10] a novel formulation of the directional derivatives of B-form polynomials in matrix form was presented. Because of its crucial role in wavefront reconstruction with splines, this formulation will be repeated here to increase the understanding of the reader.

Before introducing the formulation, however, the concept of the directional coordinate must be explained. First, let $\mathbf{u}$ be a unit vector in Cartesian $\mathbb{R}^2$, then we define $\mathbf{a} \in \mathbb{R}^3$ as the directional coordinate of $\mathbf{u}$ with respect to the triangle t. The directional coordinate $\mathbf{a}$ should be seen as the barycentric representation of the Cartesian unit vector $\mathbf{u} \in \mathbb{R}^2$ with respect to a given triangle. That is, if $\mathbf{u} = \mathbf{v} - \mathbf{w}$, with $\mathbf{v}$ and $\mathbf{w}$ vectors in Cartesian $\mathbb{R}^2$, then using the short-hand notation from (5), the directional coordinate is defined as follows:

$$\mathbf{a} := b(\mathbf{v}) - b(\mathbf{w}) \quad \in \mathbb{R}^3, \tag{24}$$

with $b(\mathbf{v})$ and $b(\mathbf{w})$ the barycentric coordinates with respect to t of $\mathbf{v}$ and $\mathbf{w}$, respectively.

Using the formulation from [10], the directional derivative of order m in the direction $\mathbf{u}$ of a B-form polynomial $p(b(\mathbf{x}))$ on a single triangle t can be expressed in terms of the original vector of B-coefficients as follows:

$$D_{\mathbf{u}}^m p(b(\mathbf{x})) = \frac{d!}{(d-m)!} \mathbf{B}^{d-m}(b(\mathbf{x})) \mathbf{P}^{d,d-m}(\mathbf{a}) \cdot \mathbf{c}^t, \tag{25}$$

with $\mathbf{P}^{d,d-m}(\mathbf{a}) \in \mathbb{R}^{\frac{(d-m+2)!}{2(d-m)!} \times \hat{d}}$ the *de Casteljau matrix* of degree d to $d-m$ from [10] expressed in terms of the directional coordinate $\mathbf{a}$ of $\mathbf{u}$ with respect to the triangle t. In (25), $\mathbf{B}^{d-m}(b(\mathbf{x}))$ is the vector of basis polynomials from (13) for degree $d - m$, and $\mathbf{c}^t$ is the vector of B-coefficients for a single triangle from (14).

It will be shown in the next section that (25) is the key to spline based wavefront reconstruction, because it directly relates the spline function model of the wavefront to its directional derivatives modeling the slopes and curvatures in terms of $\mathbf{c}^t$.

For example, in the case of the first order directional derivative of a simplex B-spline $p(b(\mathbf{x}))$ of degree 1 on a single triangle, (25) can be simplified as follows:

$$D_u^1 p(b(\mathbf{x})) = \mathbf{B}^0(b(\mathbf{x})) \mathbf{P}^{1,0}(\mathbf{a}) \cdot \mathbf{c}^t, \tag{26}$$

which for $\mathbf{b}, \mathbf{a} \in \mathbb{R}^3$ reduces to:

$$D_{\mathbf{u}}^1 p(b(\mathbf{x})) = \begin{cases} \begin{bmatrix} a_0 & a_1 & a_2 \end{bmatrix} \cdot \mathbf{c}^t & , \mathbf{x} \in t, \\ 0 & , \mathbf{x} \notin t. \end{cases} \tag{27}$$

Before continuing, a full-triangulation formulation of de Casteljau matrix for a triangulation $\mathcal{T}_J$ of the form (6) consisting of J triangles needs to be defined. For a single observation, this full-triangulation formulation is a block diagonal matrix with a total of J blocks of the form $\mathbf{P}^{d,d-m}(\mathbf{a_u})$ on the main diagonal, with $j = 1, 2, \ldots, J$:

$$\mathbf{P}_{\mathbf{u}}^{d,d-m} := \mathrm{diag}\left(\mathbf{P}_j^{d,d-m}(\mathbf{a_u})\right)_{j=1}^{J} \quad \in \mathbb{R}^{J\frac{(d-m+2)!}{2(d-m)!} \times J\hat{d}}, \tag{28}$$

where $\mathbf{a_u}$ is the directional coordinate of the derivative direction $\mathbf{u}$ with respect to the triangle t_j.

The full triangulation form of the directional derivative of the simplex B-spline for a single observation $b(\mathbf{x})$ then follows from the combination of (16), (28), and (17):

$$D_{\mathbf{u}}^m s_d^r(b(\mathbf{x})) = \frac{d!}{(d-m)!} \mathbf{B}^{d-m} \mathbf{P}_{\mathbf{u}}^{d,d-m} \cdot \mathbf{c}, \tag{29}$$

3. Wavefront reconstruction with simplex B-splines

In this section the SABRE method for wavefront reconstruction is introduced and connected to the literature. Additionally, we show that the SABRE is not subject to the waffle mode. Finally, the steps that make up the SABRE algorithm are presented, its computational aspects are discussed, and a tutorial example is given.

3.A. Wavefront reconstruction from slope measurements

The relationship between the slopes of the wavefront phase and the wavefront phase can be described in the form of the following system of first order partial differential equations [15]:

$$\begin{aligned}
\sigma_x(x,y) &= \frac{\partial \phi(x,y)}{\partial x}, \\
\sigma_y(x,y) &= \frac{\partial \phi(x,y)}{\partial y},
\end{aligned} \tag{30}$$

with $\phi(x,y)$ the unknown wavefront, and with $\sigma_x(x,y)$ and $\sigma_y(x,y)$ the wavefront slopes at (x,y) in the directions x and y, respectively.

3.B. Wavefront reconstruction with the finite difference method

One of the best known zonal methods for the reconstruction of wavefronts from wavefront slopes is the finite difference (FD) method. The FD method comes in a number of different specific forms which depend on the sampling geometry, such as the Fried [12], Hudgin [17], and Southwell [29] geometries. All FD methods have in common that they reduce (30) into a discrete form which solution is approximated with linear interpolating polynomials [15].

In order to connect the SABRE method with the literature we shall compare it directly with the Fried form of the FD method [12,29]. The Fried FD sensor model assumes that the

average slope in a grid cell formed by four phase points is equal to the average difference in phase between the phase points, see Fig. 3. The Fried sensor model is:

$$
\begin{aligned}
\sigma_x(i,j) &= \left[(\phi(i+1,j) - \phi(i,j)) + \right. \\
&\qquad \left. (\phi(i+1,j+1) - \phi(i,j+1)) \right] / (2h) + n_x(i,j) \\
\sigma_y(i,j) &= \left[(\phi(i,j+1) - \phi(i,j)) + \right. \\
&\qquad \left. (\phi(i+1,j+1) - \phi(i+1,j)) \right] / (2h) + n_y(i,j)
\end{aligned}
\tag{31}
$$

with h the step size between phase points, with $n_x(i,j)$ and $n_y(i,j)$ residual terms that contain both noise and modeling errors. The indices $i = 1, 2, \ldots, M-1$, and $j = 1, 2, \ldots, N-1$ are grid coordinates on the grid domain $\Omega(M,N)$, which is defined as follows:

$$
\Omega(M,N) \in \mathbb{R}^2, \quad M, N \in \mathbb{N}
\tag{32}
$$

By enumerating all $M \cdot N$ phase points $\phi(i,j)$ into a single row vector $\boldsymbol{\phi}$, and by using all slope measurements, the following matrix equation can be constructed:

$$
\boldsymbol{\sigma} = \mathbf{G}\boldsymbol{\phi} + \mathbf{n}
\tag{33}
$$

with $\boldsymbol{\sigma} = \begin{bmatrix} \boldsymbol{\sigma}_x^\top & \boldsymbol{\sigma}_y^\top \end{bmatrix}^\top$ the vector of slope measurements which is constructed by appending the vector of all slopes in the x-direction with the vector of all slopes in the y-direction. The matrix $\mathbf{G}$ is the geometry matrix which is constructed such that each row multiplied with $\boldsymbol{\phi}$ results in a single expression of the form (31).

Based on (33), an estimate for the global wavefront $\hat{\boldsymbol{\phi}}$ can now be obtained using any parameter estimation technique, see e.g. [11, 15, 30, 31]. For example, the ordinary least squares estimator for $\boldsymbol{\phi}$ is:

$$
\hat{\boldsymbol{\phi}}_{FD} = \mathbf{G}^+ \boldsymbol{\sigma}
\tag{34}
$$

with $\mathbf{G}^+$ the Moore-Penrose pseudo inverse of $\mathbf{G}$ as $\mathbf{G}^\top\mathbf{G}$ is singular in general [2]. In particular, for the Southwell FD geometry, the nullspace of $\mathbf{G}^\top\mathbf{G}$ has dimension 1 (piston mode), while for the Fried FD geometry, the nullspace has dimension 2 (piston mode and waffle mode) [24, 32]. The matrix $\mathbf{G}^+$ is the FD *reconstruction matrix*, which is computed only once for a given FD sensor geometry.

3.C. *Wavefront reconstruction with the SABRE*

The main contribution of this paper is the SABRE, which is a new method for wavefront reconstruction that uses the basis functions of bivariate simplex B-splines to locally model the wavefront using local WFS measurements. The SABRE can be seen as a generalization of the FD method to the nonlinear case, see Sec. 6.

The approach taken with the SABRE method differs from the FD method in the sense that it is assumed that the unknown wavefront $\phi(x, y)$ can be approximated with a parametrized model in the form of a bivariate simplex B-spline of degree $d \geq 1$ and continuity order r from (15):

$$\phi(x, y) \approx s_r^d(b(x, y)) = \mathbf{B}^d(b(x, y)) \cdot \mathbf{c}, \quad d \geq 1, \ (x, y) \in t \tag{35}$$

The right hand side of (35) then is the SABRE model that approximates the wavefront $\phi(x, y)$.

Under the assumption that (35) holds, we can then use (25) to rewrite (30) into the following slope sensor model:

$$\begin{aligned}
\sigma_x(x, y) &= \tfrac{d!}{(d-1)!} \mathbf{B}^{d-1}(b(x, y)) \mathbf{P}^{d,d-1}(\mathbf{a_x}) \cdot \mathbf{c}^t + \nu_x(x, y), \\
\sigma_y(x, y) &= \tfrac{d!}{(d-1)!} \mathbf{B}^{d-1}(b(x, y)) \mathbf{P}^{d,d-1}(\mathbf{a_y}) \cdot \mathbf{c}^t + \nu_y(x, y),
\end{aligned}$$

$$\tag{36}$$

with $d \geq 1$ the polynomial degree of the spline, and with $\mathbf{a_x}$ and $\mathbf{a_y}$ the directional coordinates respectively of $\mathbf{u_x}$ and $\mathbf{u_y}$ with respect to the triangle t. The terms $\nu_x(x, y)$ and $\nu_y(x, y)$ in (36) are residual terms which contain both the sensor noise as well as the modeling errors.

Use of the SABRE method requires the introduction of a new sensor geometry that is triangular in nature. In Fig. 3 the basic SABRE sensor geometry is compared to that of the Southwell and Fried FD sensor geometries. In Table 1 the properties of the different SABRE geometries are shown. The fundamental difference between the FD and the SABRE methods is that for all FD methods the wavefront phase is defined only at the grid locations $(m, n) \in \mathbb{N}^2$, while for the SABRE method the phase is defined at any location $(x, y) \in \mathcal{T}$. The result is that the SABRE method allows for the decoupling between slope measurement locations and phase point locations.

3.D. The anchor constraint

Before continuing with the definition of the SABRE, a new type of constraint is introduced in the form of the anchor constraint. Effectively, the anchor constraint predefines the value of the unknown constant of integration (i.e. the *piston mode*) that arises when solving the first order PDE from (30). The anchor constraint is essential for producing a well-conditioned parameter estimation problem for the B-coefficients of the SABRE model.

The anchor constraint is derived as follows. First, we reformulate (29) with $m = 1$ in integral form as follows:

$$\begin{aligned}
\int_{\mathcal{T}} D_{\mathbf{u}}^1 s_r^d(b(\mathbf{x})) d\mathbf{u} &= \int_{\mathcal{T}} d\mathbf{B}^{d-1} \mathbf{P}^{d,d-m} \mathbf{c} \, d\mathbf{u}, \\
&= \mathbf{B}^d \mathbf{c} + k, \tag{37}
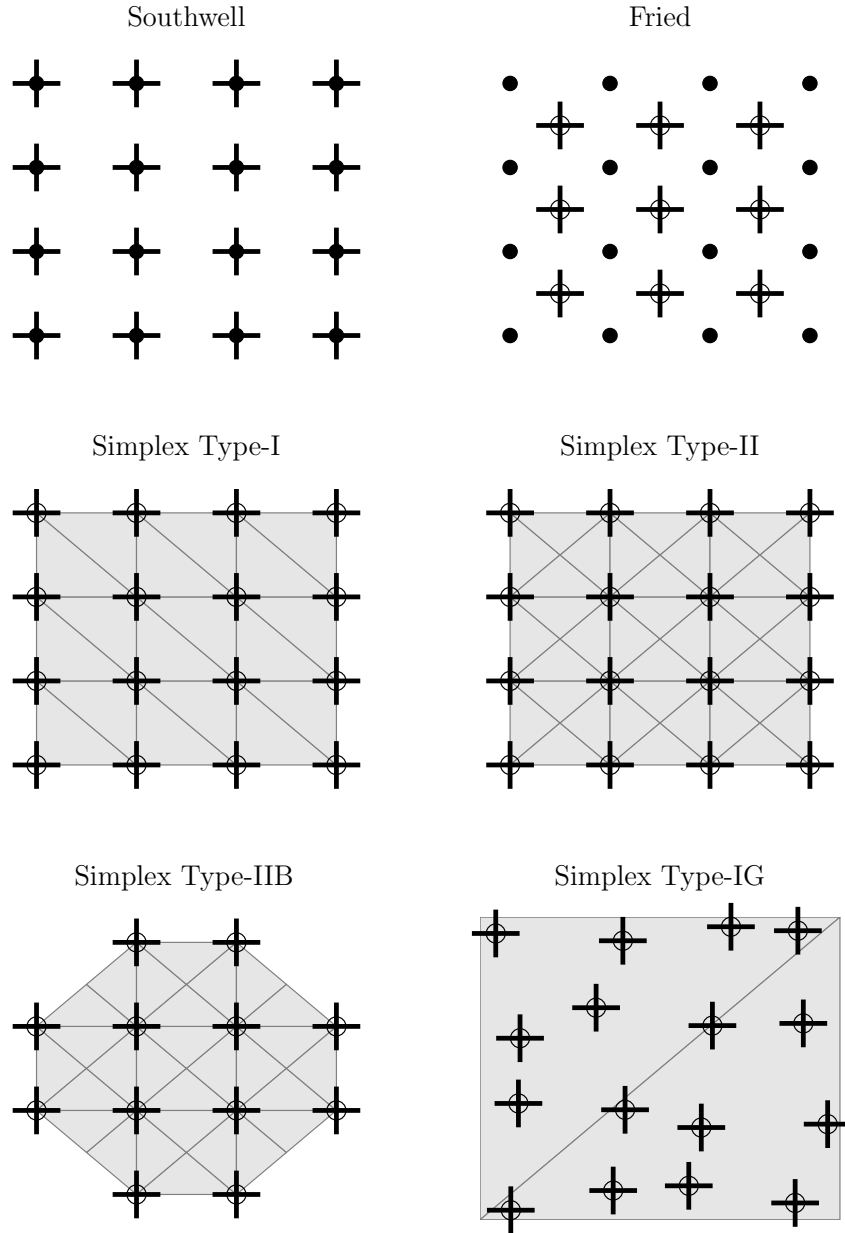\end{aligned}$$

Fig. 3: Southwell geometry (top left) and Fried (top right) sensor geometries compared with 4 different SABRE geometries (middle and bottom rows). Black dots are the phase point locations, horizontal and vertical lines are the slope measurements in the x and y directions, respectively. The open circles are the locations of the slope measurements. Gray lines in the SABRE geometries are the triangle edges, while the shaded area inside the triangulations is the area in which $\phi(x, y)$ is defined.

Sensor geometry	Triangulation Type	Rectangular domain	Data at vertices
Type-I	I	yes	yes
Type-IG	I	yes	no
Type-IB	I	no	yes
Type-IBG	I	no	no
Type-II	II	yes	yes
Type-IIG	II	yes	no
Type-IIB	II	no	yes
Type-IIBG	II	no	no

Table 1: Properties of SABRE geometries

with k an unknown constant that is proportional to the piston mode. The resulting spline model for the wavefront then is:

$$s_d^r(b(\mathbf{x})) = \mathbf{B}^d \mathbf{c} + k. \tag{38}$$

The affine property of the B-coefficients allows us to rewrite (38) as follows:

$$s_d^r(b(\mathbf{x})) = \mathbf{B}^d(\mathbf{c} + k \cdot \mathbb{1}). \tag{39}$$

with $\mathbb{1} \in \mathbb{R}^{J \cdot \hat{d} \times 1}$ a row vector containing only 1's.

The global B-coefficient vector can be partitioned into two parts; the first part containing only the first B-coefficient, and the second part the remainder of B-coefficients:

$$\mathbf{c} = \left[\begin{array}{c} c_{d,0,0}^{t_1} + k \\ \tilde{\mathbf{c}} + k \cdot \mathbb{1} \end{array} \right], \tag{40}$$

with $\mathbb{1} \in \mathbb{R}^{(J \cdot \hat{d} - 1) \times 1}$.

The anchor constraint then is the following:

$$k = -c_{d,0,0}^{t_1}, \tag{41}$$

Substitution of (41) in (39) then results in the SABRE model with fixed piston mode:

$$s_d^r(b(\mathbf{x})) = \mathbf{B}^d \cdot \left[\begin{array}{c} 0 \\ \tilde{\mathbf{c}} - c_{d,0,0}^{t_1} \cdot \mathbb{1} \end{array} \right], \tag{42}$$

15

In the following, we require a vector form of the anchor constraint. If $\mathbf{h} = [1\ 0\ \cdots\ 0]$ is the *anchor vector*, the anchor constraint becomes:

$$\mathbf{h} \cdot \left[(c_{d,0,0}^{t_1} + k)\ \ (\tilde{\mathbf{c}} + k \cdot \mathbb{1})^\top \right]^\top = 0. \tag{43}$$

3.E. Linear SABRE

The linear SABRE problem for a total of K slope measurements on a complete triangulation consisting of J triangles is derived from (36) as follows:

$$
\begin{aligned}
\sigma &= \mathbf{B}^0 \mathbf{P_u}^{1,0} \mathbf{c} + \mathbf{n}, \\
0 &= \mathbf{A}\mathbf{c},
\end{aligned} \tag{44}
$$

with $\sigma \in \mathbb{R}^{K \times 1}$ the vector of measured wavefront slopes, with $\mathbf{B}^0 \in \mathbb{R}^{K \times J}$ the global matrix of basis polynomials from (16) of polynomial degree 0, with $\mathbf{P_u}^{1,0} \in \mathbb{R}^{J \times 3J}$ the de Casteljau matrix from (28), and with $\mathbf{c} \in \mathbb{R}^{3J \times 1}$ the global vector of B-coefficients from (17). The matrix $\mathbf{A}$ in (44) is a constraint matrix defined as follows:

$$\mathbf{A} := \begin{bmatrix} \mathbf{H} \\ \mathbf{h} \end{bmatrix} \in \mathbb{R}^{(EV+1) \times J\hat{d}} \tag{45}$$

with $\mathbf{H} \in \mathbb{R}^{(EV) \times J\hat{d}}$ the smoothness matrix from (23), and with $\mathbf{h} \in \mathbb{R}^{1 \times J\hat{d}}$ the anchor constraint from (43).

For a single triangle t, the slope equation from (44) can be simplified using (27):

$$
\begin{aligned}
\sigma_x(x,y) &= a_{x_0}c_{1,0,0} + a_{x_1}c_{0,1,0} + a_{x_2}c_{0,0,1} + n_x(x,y), \\
\sigma_y(x,y) &= a_{y_0}c_{1,0,0} + a_{y_1}c_{0,1,0} + a_{y_2}c_{0,0,1} + n_y(x,y),
\end{aligned} \tag{46}
$$

with $(a_{x_0}, a_{x_1}, a_{x_2})$ the directional coordinates of a vector $\mathbf{u}_x = (1,0)$ in the x-direction, and with $(a_{y_0}, a_{y_1}, a_{y_2})$ the directional coordinates of a vector $\mathbf{u}_y = (0,1)$ in the y direction, all with respect to t. Note that the SABRE model does not depend on the location (x,y); the wavefront slope is assumed to be constant over the complete triangle.

3.F. Nonlinear SABRE

The nonlinear SABRE problem follows from extending the per-triangle nonlinear sensor model from (36) into the following full triangulation form for all K slope and L curvature measurements:

$$
\begin{aligned}
\sigma &= d\mathbf{B}^{d-1}\mathbf{P_u}^{d,d-1}\mathbf{c} + \mathbf{n}, \\
0 &= \mathbf{A}\mathbf{c},
\end{aligned} \tag{47}
$$

16

with $\boldsymbol{\sigma} \in \mathbb{R}^{K \times 1}$ the vector of measured wavefront slopes, and with $\mathbf{c} \in \mathbb{R}^{J\hat{d} \times 1}$ the global vector of B-coefficients from (17). The matrices of basis functions in (47) are constructed according to (16), while the de Casteljau matrices are constructed using (28). Finally, the constraint matrix $\mathbf{A}$ in (47) is constructed using (45).

An important implication of nonlinear SABRE is that the SABRE model is a function of the geometric location of the slope measurements (i.e. (x, y)). The reason for this is that the matrix with B-form regressors $\mathbf{B}^{d-1}$ in (47) for $d \geq 2$ depends on the (barycentric) location of the slope measurement $b(x, y)$.

For example, if we assume a quadratic polynomial model structure for the wavefront, that is, $\phi(x, y) \approx \mathbf{B}^2 \mathbf{c}^t$, the slope equation in (47) becomes:

$$\boldsymbol{\sigma} = 2\mathbf{B}^1 \mathbf{P}_{\mathbf{u}}^{2,1} \mathbf{c} + \mathbf{n}. \tag{48}$$

For a single triangle t, (48) can be expanded as follows:

$$
\begin{aligned}
\sigma_x(x, y) &= 2b_0 \left(a_{x_0} c_{2,0,0} + a_{x_1} c_{1,1,0} + a_{x_2} c_{1,0,1} \right) \\
&\quad + 2b_1 \left(a_{x_0} c_{1,1,0} + a_{x_1} c_{0,2,0} + a_{x_2} c_{0,1,1} \right) \\
&\quad + 2b_2 \left(a_{x_0} c_{1,0,1} + a_{x_1} c_{0,1,1} + a_{x_2} c_{0,0,2} \right) \\
&\quad + n_x(x, y), \\
\sigma_y(x, y) &= 2b_0 \left(a_{y_0} c_{2,0,0} + a_{y_1} c_{1,1,0} + a_{y_2} c_{1,0,1} \right) \\
&\quad + 2b_1 \left(a_{y_0} c_{1,1,0} + a_{y_1} c_{0,2,0} + a_{y_2} c_{0,1,1} \right) \\
&\quad + 2b_2 \left(a_{y_0} c_{1,0,1} + a_{y_1} c_{0,1,1} + a_{y_2} c_{0,0,2} \right) \\
&\quad + n_y(x, y),
\end{aligned}
\tag{49}
$$

with $b(x, y) = (b_0, b_1, b_2)$ the barycentric coordinate of the Cartesian point (x, y) with respect to t. Clearly, (49) is dependent on the actual location of the slope measurement inside the triangle.

3.G. Generalized SABRE

As a final generalization, the SABRE method enables the use of the resultant directional derivative instead of the set of directional derivatives in the x and y directions, see Fig. 4. In this case, the two-component PDE from (36) can be replaced with a single PDE defined in the general direction u as follows:

$$\sigma_{\mathbf{u}}(x, y) = \frac{d!}{(d-1)!} \mathbf{B}^{d-1}(b(x, y)) \mathbf{P}^{d, d-1}(\mathbf{a_u}) \cdot \mathbf{c}^t + n(x, y), \tag{50}$$

with $\mathbf{u}$ a Cartesian vector in $\mathbb{R}^2$, and with $\mathbf{a_u}$ the corresponding directional coordinate in barycentric $\mathbb{R}^3$. The advantage of (50) is that compared to the two-component PDE from
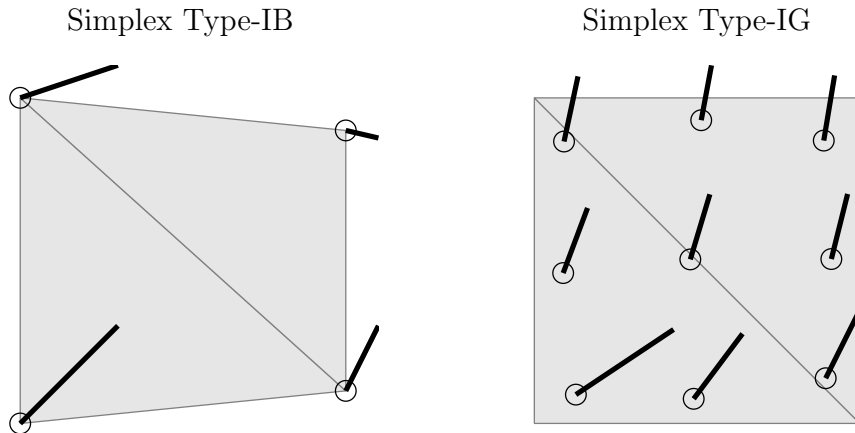
Fig. 4: General Simplex Type-IB geometry (left) and Simplex Type-IG geometry (right). Open circles are the lenslet apertures.

(36) it requires only half the number of slope measurements. This translates into lower computational and memory loads during the construction of the reconstruction matrix. The disadvantage of (50), however, is that **u** will vary for time-varying wavefronts, requiring a complete rebuild of the reconstruction matrix at each time step.

3.H. A least squares estimator for the B-coefficients

In this paragraph a least squares (LS) estimator is presented for the B-coefficients of the SABRE model approximating a wavefront using wavefront slope measurements.

The LS estimator requires that the constraint equations in (44) and (47) are eliminated from the system by projection on the nullspace of the constraint matrix **A** from (45). In that case, the wavefront reconstruction problem can be formulated in the form of an unconstrained linear regression problem as follows:

$$\sigma = \mathbf{Dc} + \mathbf{n}, \tag{51}$$

with **n** a vector containing Gaussian distributed white noise and with **D** the system matrix given by:

$$\mathbf{D} = d\mathbf{B}^{d-1}\mathbf{P}_{\mathbf{u}}^{d,d-1}\mathbf{N_A} \tag{52}$$

with $\mathbf{N_A}$ a basis for $null(\mathbf{A})$. The matrix **D** in (51) is the SABRE equivalent of the FD geometry matrix **G** from (33).

The OLS cost function in terms of the B-coefficients is:

$$J(\mathbf{c}) = \left(\sigma^\top - \mathbf{D}\mathbf{c}\right)^\top \left(\sigma^\top - \mathbf{D}\mathbf{c}\right), \tag{53}$$

The LS estimator for the B-coefficients of the SABRE model is:

$$\begin{aligned}
\hat{\mathbf{c}}_{LS} &= \mathbf{N_A}(\mathbf{D}^\top\mathbf{D})^{-1}\mathbf{D}^\top\sigma, \\
&= \mathbf{Q}\sigma, \tag{54}
\end{aligned}$$

with $\mathbf{Q} = \mathbf{N_A}(\mathbf{D}^\top\mathbf{D})^{-1}\mathbf{D}^\top$ the SABRE *reconstruction matrix*, which is computed only once for a given geometry. Matrix $\mathbf{D}^\top\mathbf{D}$ is guaranteed to be of full rank, and therefore has an empty null-space. This is in contrast with the FD equivalent $\mathbf{G}^\top\mathbf{G}$ from (33) which in general has a rank deficiency of 2, and consequently a 2-dimensional null-space. As a result the SABRE has a predefined piston mode through the anchor constraint, and is not subject to the waffle mode through the action of the continuity constraints.

Note that the matrix $\mathbf{D}^\top\mathbf{D}$ is invertible, which is a direct result of the use of the anchor constraint from (43) together with the smoothness constraints from (23).

Using (54) the resulting least squares SABRE model is:

$$\hat{\phi}_{LS}(\mathbf{x}) = \mathbf{B}^d\hat{\mathbf{c}}_{LS}. \tag{55}$$

3.I. The SABRE algorithm

The SABRE algorithm consists of two parts; an initialization part and a real-time part. The SABRE algorithm differs from the FD reconstruction algorithm only during the initialization part in which the SABRE reconstruction matrix is determined. The initialization part of the SABRE algorithm consists of the following 4 steps:

Input The inputs to the algorithm are the SABRE model structure in the form of the triangulation type (see Table 1), the spline degree d and the continuity order r. Additionally, a reference WFS image is supplied, and the user specifies a parameter estimator.

Step 1 The reference centers of the SH lenslet array are determined using the reference WFS image. A triangulation $\mathcal{T}_J$ of the type specified by the user is created by triangulating the reference centers using a (Delaunay) triangulation algorithm.

Step 2 The system of equations from (47) are formulated. For this, the matrix with B-form regressors $\mathbf{B}^{d-1}$ from (16), and the global de Casteljau matrix $\mathbf{P}_{\mathbf{u}}^{d,d-1}$ from (28) are constructed. The constraint matrix $\mathbf{A}$ from (45) is assembled using the smoothness matrix $\mathbf{H}$ from (23) and the anchor constraint $\mathbf{h}$ from (43). A basis for the null space of $\mathbf{A}$ is calculated.

19

Step 3 The system matrix $\mathbf{D}$ is constructed using (52), and the problem is stated in the linear regression form from (51).

Step 4 The SABRE reconstruction matrix $\mathbf{Q}$ is calculated based on the choice of parameter estimator. In the case of an LS estimator, $\mathbf{Q}$ is constructed according to (54).

The real-time part of the SABRE algorithm uses the SABRE reconstruction matrix $\mathbf{Q}$ in an matrix-vector-multiplication (MVM) operation to reconstruct the wavefront phase from the SH slope measurements.

3.J. Computational aspects of the SABRE

An important aspect of any WFR method is its computational complexity. While it is not the main emphasis of this paper, some basic indications of the computational complexity of the SABRE method will be given here together with some pointers to a more efficient distributed SABRE (i.e. D-SABRE) method. In the form presented in this paper, the SABRE method has a computational complexity that is of the same order as that of the FD method, i.e., $O(N^3)$ for the construction of the reconstruction matrix, and $O(N^2)$ for the reconstruction itself.

In particular, the computational complexity of the SABRE method is $O((\text{rank } \mathbf{N_A})^3)$ for the construction of the reconstruction matrix, and $O((\text{rank } \mathbf{N_A})^2)$ for the wavefront reconstruction operation, with $\mathbf{N_A}$ a basis for the nullspace of the constraint matrix $\mathbf{A}$ from (45). The rank of $\mathbf{N_A}$ in turn is a function of the total number of triangles and internal triangle edges in a triangulation and the degree and continuity order of the SABRE model.

However, the local nature of the basis functions of the simplex B-splines enable the definition of a D-SABRE method which solves the global $N \times N$ WFR problem by splitting it into G parts. Each of the G parts is formed by a sub-triangulation of the global triangulation, and the WFR problem is solved for each sub-triangulation individually using only local sensor data. This would reduce the computational complexity of the reconstruction problem from $O(N^2)$ to $O(N^2/G^2)$ when run on G parallel processors, leading to a speedup factor of $O(G^2)$ over the ordinary global SABRE method.

3.K. An example of the linear SABRE

In this paragraph we will present a tutorial example of the linear SABRE method. In the example, we use the Simplex Type-I sensor geometry from Fig. 3. We assume that there are two wavefront slope sensor apertures at which the local wavefront slope in the (x, y) directions is measured. Furthermore, we assume a linear SABRE model structure of the form (44). The corresponding spline function is defined on a triangulation consisting of 2 triangles, with a symmetric B-net orientation, see Fig. 5. Furthermore, we assume a linear SABRE model of
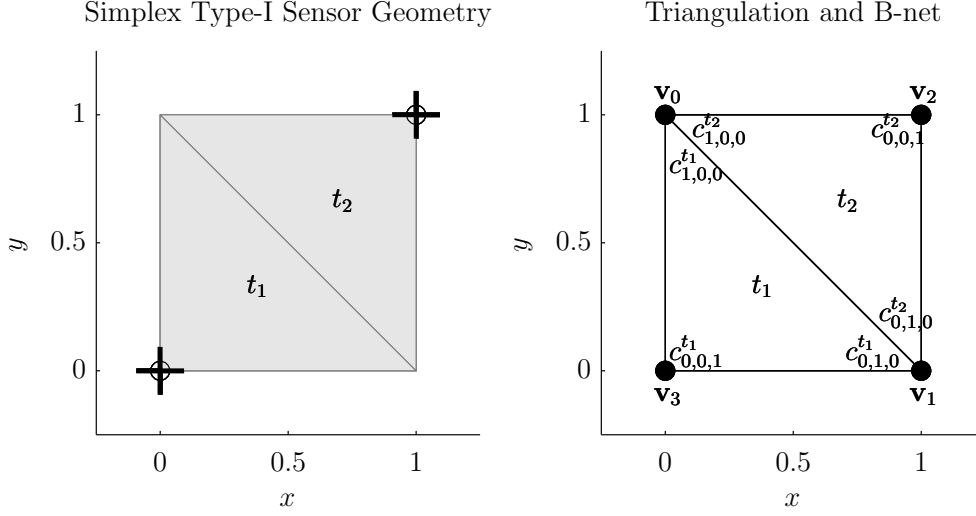
Fig. 5: A Simplex Type-I sensor geometry (left) and the triangulation and B-net for a linear simplex B-spline function (right).

the form (44). The corresponding spline function is defined on a triangulation consisting of 2 triangles, with a symmetric B-net orientation, see Fig. 5.

Before starting with the reconstruction, the various entities in (44) must be declared. We start with the vector of B-coefficients, which in this case consists of 6 B-coefficients:

$$\mathbf{c} = \begin{bmatrix} c_{1,0,0}^{t_1} & c_{0,1,0}^{t_1} & c_{0,0,1}^{t_1} & c_{1,0,0}^{t_2} & c_{0,1,0}^{t_2} & c_{0,0,1}^{t_2} \end{bmatrix}^{\top}$$

The construction of the de Casteljau matrix $\mathbf{P}^{1,0}$ from (44) requires us to first define directional coordinates for the x and y directions for each of the two triangles. Using (24), we find for the directional coordinates $\mathbf{a}_{\mathbf{x}}^{\mathbf{t_1}}$ and $\mathbf{a}_{\mathbf{y}}^{\mathbf{t_1}}$ with respect to t_1 and the directional coordinates $\mathbf{a}_{\mathbf{x}}^{\mathbf{t_2}}$ and $\mathbf{a}_{\mathbf{y}}^{\mathbf{t_2}}$ with respect to t_2:

$$\begin{aligned} \mathbf{a}_{\mathbf{x}}^{\mathbf{t_1}} &= \begin{bmatrix} 0 & 1 & -1 \end{bmatrix}^{\top}, & \mathbf{a}_{\mathbf{y}}^{\mathbf{t_1}} &= \begin{bmatrix} 1 & 0 & -1 \end{bmatrix}^{\top}, \\ \mathbf{a}_{\mathbf{x}}^{\mathbf{t_2}} &= \begin{bmatrix} -1 & 0 & 1 \end{bmatrix}^{\top}, & \mathbf{a}_{\mathbf{y}}^{\mathbf{t_2}} &= \begin{bmatrix} 0 & -1 & 1 \end{bmatrix}^{\top}, \end{aligned} \qquad (56)$$

Using (56), together with (27), the full-triangulation de Casteljau matrix $\mathbf{P}^{1,0}$ is:

$$\mathbf{P}^{1,0} = \begin{bmatrix} 0 & 1 & -1 & 0 & 0 & 0 \\ -1 & 0 & 1 & 0 & 0 & 0 \\ 0 & 0 & 0 & 1 & 0 & -1 \\ 0 & 0 & 0 & 0 & -1 & 1 \end{bmatrix},$$

We have 2 continuity conditions of the form (21): $-c_{1,0,0}^{t_1} + c_{1,0,0}^{t_2} = 0$ and $-c_{0,1,0}^{t_1} + c_{0,1,0}^{t_2} = 0$,

which lead to the smoothness matrix $\mathbf{H}$ given by:

$$\mathbf{H} = \begin{bmatrix} -1 & 0 & 0 & 1 & 0 & 0 \\ 0 & -1 & 0 & 0 & 1 & 0 \end{bmatrix}. \tag{57}$$

The anchor constraint is constructed using (41):

$$\mathbf{h} = \begin{bmatrix} 1 & 0 & 0 & 0 & 0 & 0 \end{bmatrix}. \tag{58}$$

The complete constraint matrix $\mathbf{A}$ is formed by combining (57) with (58) as shown in (45). We now proceed with reformulating the constrained model structure from (44) into the equivalent constrained form from (51) by use of the following basis for the null space of $\mathbf{A}$:

$$\mathbf{N_A} = \begin{bmatrix} 0 & 0 & -1 & 0 & 0 & 0 \\ 0 & 1 & 0 & 0 & 1 & 0 \\ 0 & 0 & 0 & 0 & 0 & 1 \end{bmatrix}^{\top}.$$

We are now ready to define the reduced regression matrix $\mathbf{D}$ from (51):

$$\mathbf{D} = \mathbf{P}^{1,0}\mathbf{N_A} = \begin{bmatrix} 1 & 1 & 0 \\ -1 & 0 & 0 \\ 0 & 0 & -1 \\ 0 & -1 & 1 \end{bmatrix},$$

which we can use to define a least squares estimator for $\mathbf{c}$ using (54).

4. Simulations with the SABRE

In this section the wavefront reconstruction performance of the SABRE method is compared to that of the Southwell and Fried FD methods in three numerical experiments utilizing a Fourier optics based Shack-Hartmann (SH) wavefront sensor simulation.

4.A. Setup of the numerical experiments

For the experiments, simulated turbulence phase screens are used in combination with a Fourier optics based SH WFS simulation to generate simulated wavefront phase slope measurements. The simulated SH WFS sensor effectively performs a local spatial averaging of the wavefront at each lenslet.

A total of 100 simulated phase screens are created using a von Kármán turbulence model [3, 4]. For the von Kármán turbulence model a turbulence outer scale of 50 m is used with a Fried coherence length of 0.2 m. The diameter of the simulated aperture is 2 m. No continuous inner scale is assumed. The average phase range for the 100 phase screens is 23 rad. The wavefront reconstruction takes place on the grid $\mathcal{X}_r$ which is of the same resolution

as the simulated SH lenslet array used in the simulation, i.e. 17×17. The phase screen ϕ is generated on a 272×272 grid indicated by $\mathcal{X}_{wf}$ such that each lenslet images a 16×16 segment of ϕ.

The overall quality of the reconstruction is calculated on the high resolution grid $\mathcal{X}_{wf}$. For this, the reconstructed wavefronts must be interpolated. For the SABRE method, this interpolation is implicit, as the SABRE model is an analytical function which can be evaluated at any point inside the model domain. For the FD method, two different interpolation schemes are used; a linear and a cubic interpolation scheme.

Three performance metrics are defined. The first is the estimation error which is defined as follows:

$$\epsilon = ||\hat{\phi} - \phi||, \tag{59}$$

with $\hat{\phi}$ the estimated wavefront which is interpolated on $\mathcal{X}_{wf}$. The normalized estimation error E_R is given by:

$$E_R = \frac{\epsilon}{||\phi||}. \tag{60}$$

The noise gain is the third performance metric:

$$K_\nu = \frac{\sigma_\nu}{\epsilon}, \tag{61}$$

with σ_ν the standard deviation of the measurement noise.

4.B. Fourier optics based SH simulator

In the numerical experiments, a simulated SH lenslet array is used to produce slope measurements, see Fig. 6. The SH lenslet array simulation is based on the Fresnel approximation to the Maxwell equations, and was taken from [6]. For the numerical experiments, a $K \times L = 17 \times 17$ lenslet array was used for a total of 289 lenslets. Each (circular) lenslet had a diameter of $D_l = 150~\mu m$ and a focal distance of $f = 5 \cdot 10^{-3}~m$. The observation wavelength was $\lambda = 633~nm$. For the non-rectangular WFS numerical experiments, a mask was placed on the 17×17 lenslet array, resulting in a non-rectangular array with a total of 240 lenslets.

A simulated CCD with $M \times N = 4352 \times 4352$ pixels is placed in the focal plane of the lenslet array. It is assumed that the pupil plane function of each lenslet acts on a 16×16 pixel segment of the global wavefront. In order to increase the resolution of the focal plane lenslet image, this segment is embedded at the center of a larger $M_p \times M_p = 256 \times 256$ grid containing only zeros.

The focal plane intensity function I_{kl} for each of the lenslets is then calculated as follows:

$$I_{kl} = \left| \mathcal{F}\mathcal{F} \left\{ A_{kl} \cdot e^{i \cdot \phi_{kl}} \right\} \right| \quad \in \mathbb{R}^{256 \times 256}, \tag{62}$$

with $\phi_{kl} \in \mathbb{R}^{256 \times 256}$ the wavefront phase segment imaged by the lenslet (k, l), with $A_{kl}(m, n) \in \mathbb{R}^{256 \times 256}$ the pupil mask of lenslet (k, l), and with $\mathcal{FF}$ the zero-shifted two-dimensional discrete Fourier transform.

The complete SH-array focal intensity function $I(x, y) \in \mathbb{R}^{4352 \times 4352}$ is then constructed using the lenslet intensity functions from (62) as follows:

$$I(k \cdot M_p + m, l \cdot M_p + n) = I_{kl}(m, n), \quad m = 1, 2, \ldots, M_p, \ n = 1, 2, \ldots, M_p, \tag{63}$$

with $0 \leq k < K$ and $0 \leq l < L$.

The local wavefront slope is obtained by calculating the shift of the center of mass (COM) of each lenslet image with respect to a reference COM. The COM for each lenslet image is calculated as follows:

$$
\begin{aligned}
x_{c_{kl}} &= \frac{\sum_{m=0}^{M_p-1} \sum_{n=0}^{M_p-1} m \cdot I(k \cdot M_p + m, l \cdot M_p + n)}{\sum_{m=0}^{M_p-1} \sum_{n=0}^{M_p-1} I(k \cdot M_p + m, l \cdot M_p + n)}, \\
y_{c_{kl}} &= \frac{\sum_{m=0}^{M_p-1} \sum_{n=0}^{M_p-1} n \cdot I(k \cdot M_p + m, l \cdot M_p + n)}{\sum_{m=0}^{M_p-1} \sum_{n=0}^{M_p-1} I(k \cdot M_p + m, l \cdot M_p + n)},
\end{aligned}
\tag{64}
$$

Finally, the slopes at lenslet (k, l) are calculated using the result from (64) as follows:

$$
\begin{aligned}
\sigma_{x_{kl}} &= \frac{(x_{c_{kl}} - x_{0_{kl}})}{f} + w\nu \\
\sigma_{y_{kl}} &= \frac{(y_{c_{kl}} - y_{0_{kl}})}{f} + w\nu
\end{aligned}
$$

$$\tag{65}$$

with $x_{0_{kl}}$ and $y_{0_{kl}}$ the calibrated (reference) centroid locations, with $0.01 \cdot ||\sigma|| \leq w \leq 10 \cdot ||\sigma||$ the variable noise magnitude, and with ν a uniformly distributed random number sequence in the interval $[-1 \ \ 1]$.

4.C. Reconstruction performance on rectangular SH arrays

In the first numerical experiment a quantitative comparison is made between the reconstruction performance of the SABRE and the Fried and Southwell FD methods using wavefront slope measurements obtained with the simulated 17×17 SH array described in Sec. 4.B. For the SABRE a Type-II triangulation consisting of 1024 triangles and a Type-IIG triangulation consisting of 256 triangles are used. Linear, quadratic and cubic polynomial SABRE model structures are used in the experiment. The least squares estimator from Sec. 3.H is used to estimate the B-coefficients of the SABRE models.

The reconstruction performance of the SABRE is compared with that of the Fried and Southwell FD methods for 20 different noise standard deviation values. For every noise value, the results from 100 turbulence realizations and 50 noise realizations are averaged. In total,
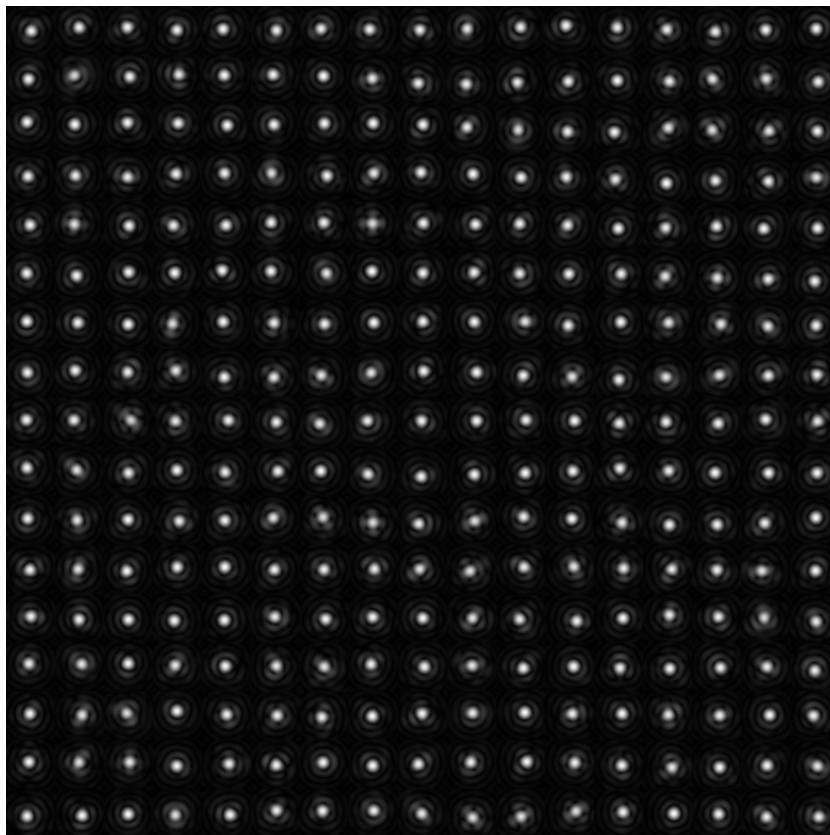
Shack-Hartmann array (17x17 lenslets) image

Fig. 6: Shack-Hartmann array image for a turbulence phase screen realization used in the numerical experiment.

there are 100000 reconstructions for each reconstruction experiment. The quality of the resulting WF models is assessed on the validation grid $\mathcal{X}_{wf}$. In Fig. 8 an example is shown of a quadratic SABRE and a linear Fried FD reconstruction of a single (zero noise) turbulence realization.

In Table 2 the normalized error E_R for the zero noise case is shown for all tested reconstruction methods. These results show that only the quadratic SABRE model with first order continuity has a lower E_R than the linear Fried FD model. On the other hand, all SABRE models have a lower E_R than the bicubic interpolated Fried FD model and the Southwell FD models.

In Fig. 9 the averaged noise gains K_ν for the SABRE and FD reconstructions are shown. A first observation shows that the quadratic and linear SABRE models outperform all FD methods in terms of K_ν for any noise level, but the difference is most pronounced for high noise levels. The cubic SABRE model has a lower noise gain than the linear FD model at low noise levels, but has a higher noise gain for $\sigma_\nu > 10$ radians. Note that the bicubic interpolated Fried FD method has a lower performance than the linear interpolated Fried FD method as well as the cubic SABRE model for all noise levels; this is due to the Lagrangian bicubcic interpolation operation which effectively smooths the Fried FD phase points with cubic polynomials of full continuity order and consequently lower approximation power than the linear Fried FD and cubic SABRE models. Note also that in Fig. 9 only the results from the linearly interpolated Southwell FD method are presented; it produced virtually identical results to its bicubic interpolated counterpart.

SABRE / FD space	rectangular domain	min (E_R)	max (E_R)
Southwell (linear)	yes	0.2127	1.2152
Southwell (cubic)	yes	0.2118	1.2738
Fried (linear)	yes	0.0533	1.5751
Fried (cubic)	yes	0.0630	1.9096
SABRE (d=1,r=0,J=1024)	yes	0.0535	1.3801
SABRE (d=1,r=0,J=816)	no	0.0523	1.4519
SABRE (d=2,r=1,J=1024)	yes	0.0525	1.4335
SABRE (d=2,r=1,J=816)	no	0.0510	1.4946
SABRE (d=3,r=1,J=256)	yes	0.0579	1.6233
SABRE (d=3,r=1,J=208)	no	0.0570	1.6929

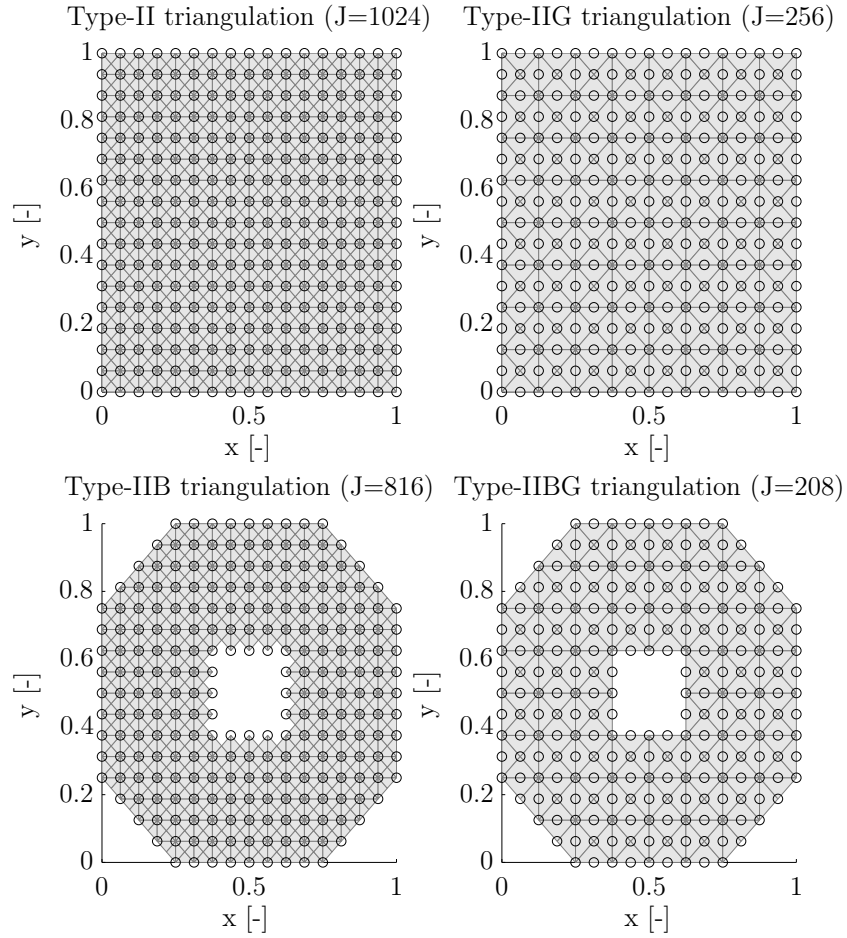Table 2: Results of the zero-noise experiments.

Fig. 7: Four SABRE sensor geometries used in the numerical experiments: A Type II geometry (top left) containing 1024 triangles, Type-IIG geometry (top right) containing 256 triangles; A Type-IIB geometry containing 816 triangles (bottom left); A Type-IIBG geometry containing 208 triangles (bottom right). The open circles are the locations of the SH-lenslets.

Turbulence phase screen

Fried FD ($E_R = 0.058$)
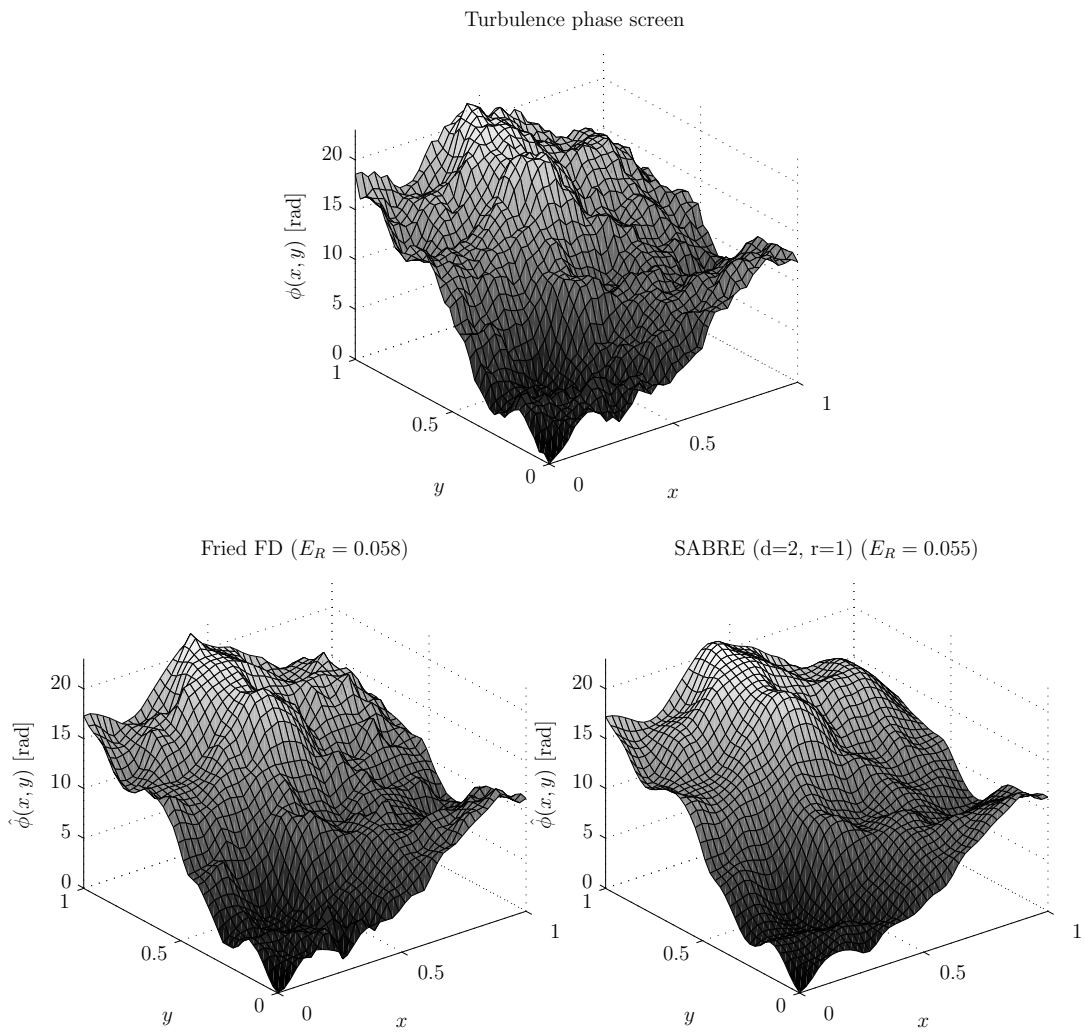
SABRE (d=2, r=1) ($E_R = 0.055$)

Fig. 8: A linear Fried FD reconstruction (bottom left) and a quadratic SABRE reconstruction (bottom right) of a turbulence phase screen.

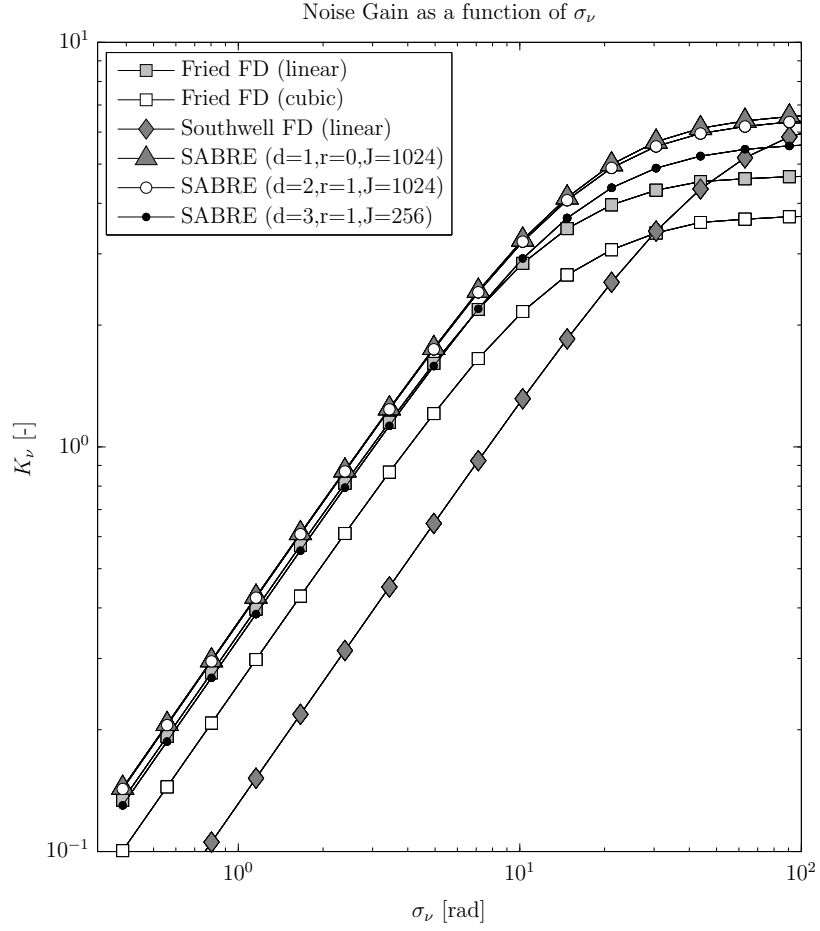Fig. 9: The noise gain K_ν as a function of the noise standard deviation σ_ν for a number of different linear and nonlinear SABRE reconstructors is compared to Fried and Southwell FD-reconstructors. A total of 100 turbulence realizations and 50 noise realizations are used for each noise setting.

4.D. Reconstruction performance on non-rectangular SH arrays

In the second numerical experiment the reconstruction performance of the SABRE on non-rectangular sensor arrays is investigated. For this experiment a octagonal mask with a central obstruction is used on the 17×17 SH array described in Sec. 4.B, see Fig. 7. The non-obscured lenslet reference centroids are triangulated with a Type-IIB consisting of 816 triangles and a Type-IIBG triangulation consisting of 208 triangles. The same linear, quadratic and cubic polynomial SABRE model structures are used as in the previous experiment. The least squares estimator from Sec. 3.H is used to estimate the B-coefficients of the SABRE models. It is important to note that the SABRE algorithm for the non-rectangular SH array is exactly equal to that of the rectangular SH array.

In Table 2 the normalized estimation errors of the non-rectangular SABRE models for the zero-noise case is presented. The SABRE models defined on the non-rectangular triangulations result in a lower normalized estimation error than SABRE models of the same degree and continuity order defined on rectangular triangulations. In Fig. 10 three plots are shown which compare the noise gain of SABRE models of equal degree and continuity order defined on rectangular and non-rectangular SH arrays. The plots show that the noise gain of SABRE models on non-rectangular arrays exceeds that of SABRE models of the same degree defined on rectangular SH arrays for all noise levels.

5. Conclusions

A new zonal method for wavefront reconstruction using multivariate simplex B-spline basis functions in a linear regression framework is introduced. This new method, indicated as the SABRE , approximates solutions to the first order partial differential equations that relate wavefront slope to the wavefront phase using bivariate simplex B-splines. While the current paper only introduces a least squares estimator for the B-coefficients of the SABRE model, the SABRE is fully compatible with any more advanced linear regression parameter estimation technique. The SABRE method is aimed at AO applications in which linear wavefront reconstruction methods can not provide the required accuracy levels at a given sensor noise level, or in AO applications in which wavefront slope or curvature measurements are made on non-rectangular, partially obstructed, and misaligned sensor grids. Furthermore, the SABRE reconstruction matrix is of full rank, and as a consequence the SABRE is not subject to the waffle mode.

The new method is compared to existing finite difference methods from the literature on both a theoretical and a numerical level. On a theoretical level it is proved that any finite difference method is a special case of a linear SABRE model with C^0 continuity on a Type-II triangulation. Additionally, we prove that the approximation power of a class of nonlinear SABRE models exceeds the approximation power of the class of linear SABRE models. This
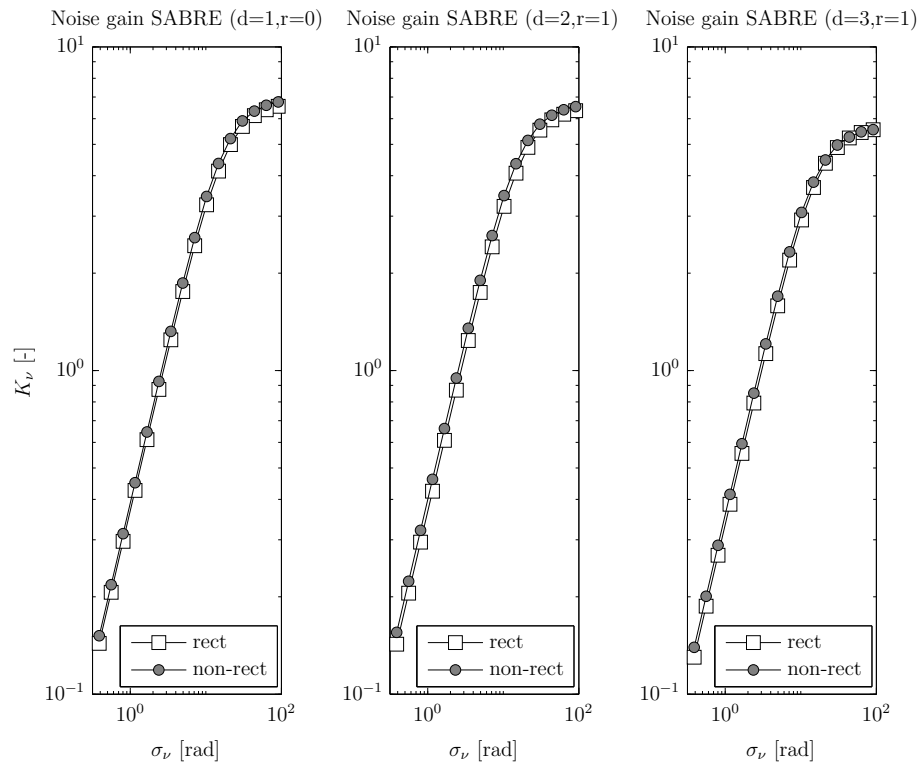
Fig. 10: An investigation of the influence of sensor geometry on the noise gain K_ν for SABRE models of equal degree and continuity order. A total of 100 turbulence realizations and 50 noise realizations are used for each noise setting.

31

class of nonlinear SABRE models will ultimately result in reconstructed wavefronts of higher accuracy than those produced by any linear SABRE, and consequently, any finite difference model.

The computational complexity of the SABRE method in its basic form is $O(N^2)$ for the reconstruction operation. This is equal to the matrix-vector-multiplication method used for the FD method. However, the local nature of the simplex B-spline basis polynomials allows the definition of a distributed SABRE (D-SABRE) algorithm which can theoretically obtain a computational complexity of $O(N^2/G^2)$ when a total of G parallel processors are used. Additionally, the sparse matrix methods from [11,30] and the multigrid preconditioned conjugate-gradient methods from [13,31] can be used with the SABRE to further increase computational efficiency.

Two numerical experiments are conducted using a Fourier optics based simulation of a Shack-Hartmann lenslet array. Both experiments use turbulence phase screens generated using a von Kármán turbulence model together with a variable magnitude sensor noise model. In the first numerical experiment, the reconstruction performance of the SABRE method is compared to that of the Fried and Southwell FD methods on rectangular SH lenslet arrays. In this experiment it is shown that a quadratic SABRE model outperforms all tested FD methods for all noise levels. In the second experiment the reconstruction performance of the SABRE on non-rectangular SH sensor arrays is investigated. It is found that reconstruction performance is not negatively influenced by the particular geometry of the underlying sensor grid.

6.   Appendix

In this appendix a theorem is provided that on a theoretical level connects the SABRE method to the FD method. In particular, it is proved that any linear FD model is in fact a special case of a linear SABRE model on a Type-II triangulation. Additionally, it is proved that there exist nonlinear SABRE models that can approximate a wavefront with higher accuracy than any linear FD method.

6.A.   The SABRE as a generalization of the FD method

In the following sections, we require a definition for the space of linear FD approximators, that is, the space which contains all possible linear FD reconstructions for a given sensor grid. We indicate this space as $\mathcal{F}_1^0(\Omega(M, N))$, and define it as follows:

Definition 1. $\mathcal{F}_1^0(\Omega(M, N))$ *is defined as the space of all linear FD approximators of continuity order C^0 on the $M \times N$ grid $\Omega(M, N)$ from (32) such that we have for every (estimated) phase point $\hat{\phi}_{FD}(x_i, y_j)$:*

$$\hat{\phi}_{FD}(x_i, y_j) \in \mathcal{F}_1^0(\Omega(M, N)), \quad 1 \leq i \leq M, 1 \leq j \leq N \tag{66}$$

The following lemma proves that any linear FD model is in fact a special case of a linear SABRE model defined on a Type-II triangulation.

Lemma 1. *Let $\mathcal{S}_1^0(\mathcal{T}_{II}(\Omega(M,N)))$ be the linear spline space of C^0 continuity defined on the Type-II triangulation $\mathcal{T}_{II}(\Omega(M,N))$ with $\Omega(M,N)$ the FD grid domain from (32). In that case, the space of FD approximators $\mathcal{F}_1^0(\Omega(M,N))$ from (66) is a subset of this spline space as follows:*

$$\mathcal{F}_1^0(\Omega(M,N)) \subset \mathcal{S}_1^0(\mathcal{T}_{II}(\Omega(M,N))). \tag{67}$$

Proof. The proof is based on the existence of an injective mapping of the FD phase points to the B-coefficients of the spline space. First, let ω be any grid cell in $\Omega(M,N)$ consisting of the four vertices $\mathcal{V}_\omega = \{\mathbf{v}_{i,j}, \mathbf{v}_{i+1,j}, \mathbf{v}_{i,j+1}, \mathbf{v}_{i+1,j+1}\}$. These vertices thus coincide exactly with the location of the FD phase points. Then, let $\mathcal{T}_4(\omega)$ be the Type-II triangulation of V_ω with vertex set $\mathcal{V}_{\mathcal{T}_4} = \{\mathcal{V}_\omega, \mathbf{v}_*\}$ in which $\mathbf{v}_*$ is an additional vertex located at the center of ω. Now let $s_1^0(x,y)$ be a linear bivariate spline function with C^0 continuity defined on $\mathcal{T}_4(\omega)$ as follows:

$$s_1^0(x,y) = \mathbf{B}^1(b(x,y))\mathbf{c}_\omega \in \mathcal{S}_1^0(\mathcal{T}_4(\omega)), \tag{68}$$

with $\mathbf{c}_\omega$ a vector of B-coefficients which can be decomposed as follows:

$$\mathbf{c}_\omega = [\mathbf{c_v}^\top \quad \mathbf{c_*}^\top]^\top \in \mathbb{R}^{12}, \tag{69}$$

with $\mathbf{c_v} \in \mathbb{R}^8$ the B-coefficients located at the vertices in $\mathcal{V}_\omega$, and with $\mathbf{c_*} \in \mathbb{R}^4$ the B-coefficients located at the center vertex $\mathbf{v}_*$.

From (21) it follows that for C^0 continuity, it is required that the values of all B-coefficients located at a vertex in $\mathcal{V}_{\mathcal{T}_4}$ are equal. As a result, we find the following for $\mathbf{c_v}$ and $\mathbf{c_*}$:

$$\begin{aligned}
\mathbf{c_v} &= [c_{\mathbf{v}_1} \quad c_{\mathbf{v}_1} \quad c_{\mathbf{v}_2} \quad c_{\mathbf{v}_2} \quad c_{\mathbf{v}_3} \quad c_{\mathbf{v}_3} \quad c_{\mathbf{v}_4} \quad c_{\mathbf{v}_4}], \\
\mathbf{c_*} &= [c_{\mathbf{v}_*} \quad c_{\mathbf{v}_*} \quad c_{\mathbf{v}_*} \quad c_{\mathbf{v}_*}],
\end{aligned} \tag{70}$$

Evaluation of the spline function (68) at any vertex $\mathbf{v}_m \in \mathcal{V}_\omega$ results in:

$$s_1^0(\mathbf{v}_m) = \mathbf{B}^1(b(\mathbf{v}_m)) \cdot \mathbf{c}_\omega = c_{\mathbf{v}_m}, \quad 1 \le m \le 4 \tag{71}$$

with $b(\mathbf{v}_m)$ the barycentric coordinate transformation of $\mathbf{v}_m$.

For the theory to hold, the FD phase points must be equal to the SABRE wavefront phase at all vertices in $\mathcal{V}_\omega$. From (71) it therefore follows that

$$\hat{\phi}_{FD}(\mathbf{v}_m) = c_{\mathbf{v}_m}, \quad 1 \le m \le 4, \tag{72}$$

with $\hat{\phi}_{FD}(\mathbf{v}_m)$ the FD wavefront phase as defined in (66).

Now let $\mathbf{c}_\phi$ be the vector of B-coefficients resulting from the substitution of the results from (72) in $\mathbf{c}_\mathbf{v}$ from (70):

$$\mathbf{c}_\phi = [\hat{\phi}_{FD}(\mathbf{v}_1) \;\; \hat{\phi}_{FD}(\mathbf{v}_1) \;\; \cdots \;\; \hat{\phi}_{FD}(\mathbf{v}_4) \;\; \hat{\phi}_{FD}(\mathbf{v}_4)], \tag{73}$$

Equation (73) implies that there exists an injective mapping of $\hat{\phi}_{FD}(\mathcal{V}_\omega)$ to $\mathbf{c}_\omega$. Evaluation of the spline function from (68) at the vertex set $\mathcal{V}_{\mathcal{T}_4}$ then results in:

$$s_1^0(\mathcal{V}_{\mathcal{T}_4}) = \mathbf{B}^1(b(\mathcal{V}_{\mathcal{T}_4})) \cdot \begin{bmatrix} \mathbf{c}_\phi \\ \mathbf{c}_* \end{bmatrix} = \begin{bmatrix} \hat{\phi}_{FD}(\mathcal{V}_\omega) \\ \mathbf{v}_* \end{bmatrix}, \tag{74}$$

with $b(\mathcal{V}_{\mathcal{T}_4})$ the transformation to barycentric coordinates of the vertices in $\mathcal{V}_{\mathcal{T}_4}$.

(74) implies that the set of all FD approximators $\hat{\phi}_{FD}(\mathcal{V}_\omega)$ is a subset of $\mathcal{S}_1^0(\mathcal{T}_4(\omega))$ for any real value of the B-coefficients $\mathbf{c}_*$ located at the center vertex $\mathbf{v}_*$:

$$\mathcal{F}_1^0(\omega) \subset \mathcal{S}_1^0(\mathcal{T}_4(\omega)). \tag{75}$$

By induction, the result from (75) can be extended to the complete domain $\Omega(M, N)$, thereby proving the lemma.

$\square$

The following lemma reproduces theorems from [21] that prove that the approximation accuracy of a given wavefront phase screen $\phi(x, y)$ with simplex B-splines depends on the spline degree as well as on the configuration of a triangulation.

Lemma 2 ([21]: Theorem 10.2, Theorem 10.6, Theorem 10.13, Theorem 10.21). *Let $\mathcal{S}_d^r(\mathcal{T}(\Omega))$ be the spline space of degree d and continuity order r defined on the triangulation $\mathcal{T}(\Omega)$ of the domain Ω. If $\phi(x, y)$ is a differentiable function with at least $d + 1$ derivatives such that $\phi(x, y) \in W_q^m(\Omega)$, with $W_q^{d+1}(\Omega)$ the Sobolev space of order m equipped with the L_q norm, then we have for the q-distance $d(\phi(x, y), S_d^r)_q$ between $\phi(x, y)$ and S_d^r:*

$$d(\phi(x, y), S_d^r)_q = \begin{cases} \mathcal{O}(|\mathcal{T}|^0) & \text{if } d < \frac{3r+2}{2}, r > 0 \\ \mathcal{O}(|\mathcal{T}|^d) & \text{if } \frac{3r+2}{2} \le d \le 2r + 1, r > 0 \\ \mathcal{O}(|\mathcal{T}|^{d+1}) & \text{if } d \ge 3r + 2, r \ge 0 \end{cases}$$

with $|\mathcal{T}|$ the longest triangle edge in the triangulation $\mathcal{T}$.

Proof. For a proof of the lemma, we refer the reader to Theorem 10.2, Theorem 10.6, Theorem 10.13, and Theorem 10.21 in [21].

$\square$

The results of **Lemma** 1 and **Lemma** 2 lead to the main theorem, which states that there exists an estimator which

the SABRE method can reconstruct the wavefront $\phi(x, y)$ with equal or higher accuracy than the FD method.

Theorem 1. *If $f \in \mathcal{F}_1^0(\Omega(M, N))$ is an FD approximator in the space of linear FD approximators from (66), then there exists a spline function $s_d^r \in \mathcal{S}_d^r(\mathcal{T}_{II}(\Omega(M, N)))$ defined on a Type-II triangulation of $\Omega(M, N)$ for which it holds that it can approximate any continuous function $\phi(x, y)$ with higher accuracy than any linear FD approximator:*

$$||\phi(x, y) - s_d^r||_q < ||\phi(x, y) - f||_q \tag{76}$$

for all $d > 1$ if $r = 0$, and for all $d \geq \frac{3r+2}{2}$ if $r > 0$.

Proof. The proof is based on the results from **Lemma** 1 and **Lemma** 2. In **Lemma** 1 it was proved that $\mathcal{F}_1^0(\Omega(M, N))$ is in fact a subset of $\mathcal{S}_1^0(\mathcal{T}_{II}(\Omega(M, N)))$, which implies the following:

$$||\phi(x, y) - s_1^0||_q \leq ||\phi(x, y) - f||_q \tag{77}$$

with $s_1^0 \in \mathcal{S}_1^0(\mathcal{T}_{II}(\Omega(M, N)))$.

Additionally, in **Lemma** 2 it was proved that the distance between $\phi(x, y)$ and $\mathcal{S}_d^r(\mathcal{T})$ depends on $|\mathcal{T}|$ as well as on d and r. In particular it was proved that

$$d(\phi(x, y), S_d^r(\mathcal{T}))_q < d(\phi(x, y), S_1^0(\mathcal{T}))_q \tag{78}$$

holds for all $d > 1$ if $r = 0$, and for all $d \geq \frac{3r+2}{2}$ if $r > 0$. Combining (77) with (78) then proves the theorem. $\square$

References

1. G. Awanou, M. J. Lai, and P. Wenston. The multivariate spline method for scattered data fitting and numerical solutions of partial differential equations. In G. Chen and M. J. Lai, editors, *Wavelets and Splines*, pages 24–75, 2005.

2. J. M. Beckers, P. Léna, O. Lai, P. Y. Madec, G. Rousset, M. Séchaud, M. J. Northcott, F. Roddier, J. L. Beuzit, F. Rigaut, and D. G. Sandler. *Adaptive Optics in Astronomy*. Cambridge University Press, 1999.

3. J. M. Conan, G. Rousset, and P. Y Madec. Wave-front temporal spectra in high-resolution imaging through turbulence. *Journal of the Optical Society of America*, 12:1559–1570, 1995.

4. R. Conan. Mean-square residual error of a wavefront after propagation through atmospheric turbulence and after correction with Zernike polynomials. *Journal of the Optical Society of America*, 25:526–536, 2008.

5. G. M. Dai. Modal wave-front reconstruction with Zernike polynomials and Karhunen-Loève functions. *Journal of the Optical Society of America*, 13:1218–1225, 1996.

6. Y. Dai, F. Li, X. Cheng, Z. Jiang, and S. Gong. Analysis on shackhartmann wave-front sensor with fourier optics. *Optics and Laser Technology*, 39:1374–1379, 2007.

7. C. de Boor. B-form basics. In G. Farin, editor, *Geometric modeling: algorithms and new trends*. SIAM, 1987.

8. C. C. de Visser. *Global Nonlinear Model Identification with Multivariate Splines*. PhD thesis, Delft University of Technology, 2011.

9. C. C. de Visser, Q. P. Chu, and J. A. Mulder. A new approach to linear regression with multivariate splines. *Automatica*, 45(12):2903–2909, 2009.

10. C. C. de Visser, Q. P. Chu, and J. A. Mulder. Differential constraints for bounded recursive identification with multivariate splines. *Automatica*, 47:2059–2066, 2011.

11. B. L. Ellerbroek. Efficient computation of minimum-variance wave-front reconstructors with sparse matrix techniques. *Journal of the Optical Society of America*, 19:1803–1816, 2002.

12. D. L. Fried. Least-square fitting a wave-front distortion estimate to an array of phase-difference measurements. *Journal of the Optical Society of America*, 67:370–375, 1977.

13. L. Gilles, C. R. Vogel, and B. L. Ellerbroek. Multigrid preconditioned conjugate-gradient method for large-scale wave-front reconstruction. *Journal of the Optical Society of America*, 19:1817–1822, 2002.

14. P. J. Hampton, P. Agathoklis, and C. Bradley. A new wave-front reconstruction method for adaptive optics systems using wavelets. *IEEE Journal of Selected Topics in Signal Processing*, 2:781–792, 2008.

15. J. Herrmann. Least-squares wave front errors of minimum norm. *Journal of the Optical Society of America*, 70:28–35, 1980.

16. X. L. Hu, D. F. Han, and M. J. Lai. Bivariate splines of various degrees for numerical solution of partial differential equations. *SIAM Journal on Scientific Computing*, 29:1338–1354, 2007.

17. R. H. Hudgin. Wavefront reconstruction for compensated imaging. *Journal of the Optical Society of America*, 67:375–378, 1977.

18. M. Kissler-Patig. Overall science goals and top level AO requirements for the E-ELT.

In *First AO4ELT conference*, 2010.

19. V. Korkiakoski and C. Vérinaud. Simulations of the extreme adaptive optics system for epics. In B. L. Ellerbroek, editor, *Adaptive Optics Systems II*, 2010.

20. M. J. Lai and L. L. Schumaker. On the approximation power of bivariate splines. *Advances in Computational Mathematics*, 9:251–279, 1998.

21. M. J. Lai and L. L. Schumaker. *Spline Functions on Triangulations*. Cambridge University Press, 2007.

22. M.J. Lai. Some sufficient conditions for convexity of multivariate Bernstein-Bézier polynomials and box spline surfaces. *Studia Scient. Math. Hung.*, 28:363–374, 1990.

23. R. J. Noll. Zernike polynomials and atmospheric turbulence. *Journal of the Optical Society of America*, 66:207–211, 1976.

24. M. D. Oliker. Sensing waffle in the fried geometry. In D. Bonaccini and R. K. Tyson, editors, *Adaptive Optical System Technologies*, volume Proc. SPIE 3353, pages 964–971, 1998.

25. L. A. Poyneer, D. T. Gavel, and J. M. Brase. Fast wave-front reconstruction in large adaptive optics systems with use of the Fourier transform. *Journal of the Optical Society of America*, 19:2100–2111, 2002.

26. L. A. Poyneer, B. A. Machintosh, and J. P. Véran. Fourier transform wavefront control with adaptive prediction of the atmosphere. *Journal of the Optical Society of America*, 24:2645–2660, 2007.

27. F. Roddier. Curvature sensing and compensation: a new concept in adaptive optics. *Applied Optics*, 27:1223–1225, 1986.

28. M. Rosensteiner. Cumulative reconstructor: fast wavefront reconstruction algorithm for extremely large telescopes. *Journal of the Optical Society of America*, 28:2132–2138, 2011.

29. W. H. Southwell. Wave-front estimation from wave-front slope measurements. *Journal of the Optical Society of America*, 79:998–1006, 1980.

30. C. R. Vogel. Sparse matrix methods for wavefront reconstruction, revisited. In *Proceedings of SPIE*, 2004.

31. C. R. Vogel and Q. Yang. Multigrid algorithm for least-squares wavefront reconstruction. *Applied Optics*, 45:705–715, 2006.

32. W. Zou and J. P. Rolland. Quantifications of error propagation in slope-based wavefront estimations. *Journal of the Optical Society of America*, 23:2629–2638, 2006.